MAX-PLANCK-INSTITUT FÜR PLASMAPHYSIK

GARCHING BEI MÜNCHEN

ANTWKB: A CODE FOR THE SIMULATION OF ION CYCLOTRON ANTENNAS IN TOKAMAKS

Marco Brambilla

IPP 5/61 April 1995

Die nachstehende Arbeit wurde im Rahmen des Vertrages zwischen dem Max-Planck-Institut für Plasmaphysik und der Europäischen Atomgemeinschaft über die Zusammenarbeit auf dem Gebiete der Plasmaphysik durchgeführt.

ABSTRACT

We have developed a code which evaluates the complex input impedance, the loading, and the spectral distribution of the launched power, of metallic antennas for ion cyclotron heating of large tokamak plasmas. The current distribution along the conductors is obtained selfconsistently from a variational method. The plasma response is evaluated assuming that the WKB approximation can be used already at the plasma edge, thereby avoiding the lengthy integration of the wave equations in the plasma. This makes possible systematic scans over frequency or other parameters, while retaining a sufficiently large number of Fourier components in the radiated fields to ensure convergence of both the resistive and reactive part of the power. Optionally, the code can evaluate the antenna response in vacuum or with a dummy load, for comparison with test bank measurements.

We have applied the code to a few antennas of practical interest. The code reproduces accurately the expected transmission-line-like behaviour of a simple feeder-to-short antenna, and reasonably well the measured properties of the folded antenna of the ASDEX Upgrade ICRF experiment. This antenna is found to have particularly favourable properties, since its outer conductors present to the plasma a relatively uniform current over a broad range of frequencies, which, moreover, is always larger than in the return conductors. The loading of the "violin antenna" recently proposed for use in ITER is found to be satisfactory in the vicinity of antenna resonances, although rather poor at other frequencies. In the case of simple strap antennas replacing the short by an adjustable capacity, as in TORE SUPRA, is confirmed to be a good way of optimizing the loading.

1 – Introduction. A sustained effort has been devoted to the theoretical description of antennas for ion cyclotron heating (ICH) in tokamaks. In a first phase, the coupling properties were investigated assuming a given, usually space-independent, distribution of currents in the external conductors [1]-[10]. This is justified as long as the antenna is electrically short, i.e. at low frequencies and in small devices. With the increase of the plasma and antenna size and the widening of the frequency range to be covered for different heating scenarios, however, the need for a self-consistent determination of the antenna currents becomes evident. A powerful variational method for the solution of the self-consistent problem was proposed by Teilhaber and Jacquinot [11] for fast-wave antennas, and extended in [12] to cover arbitrarily oriented antennas. A decisive advantage of this approach is that it provides at the same times the complex input impedance of the antenna, which is needed to treat the launcher as a known element of the h.f. circuit delivering the h.f. power from the generator to the plasma.

In large tokamaks, however, the variational approach is very computing intensive. To substantiate this statement, it is necessary to recall briefly how the coupling problem is formulated. Because of spatial dispersion, the plasma response can be evaluated in a realistic way only if the electromagnetic field can be decomposed into partial waves having a definite periodicity along the static magnetic field lines. For coupling calculations it is justified as a first approximation to neglect the curvature of the real configuration, replacing the tokamak by a plasma slab, so that this goal is easily attained by Fourier-analyzing the solution of Maxwell's equations in toroidal and poloidal directions:

$$\vec{E} = \sum_{k_y,k_z} \vec{E}(k_y, k_z, x)\, e^{i(k_y y + k_z z)} \tag{1}$$

where x, y, z are the straight geometry correspondents of the radial, poloidal and toroidal coordinates, respectively, and the summation is over a sufficiently large set of values of k_y, k_z, usually discretized according to the periodicity of the toroidal configuration:

$$k_y = \frac{m}{a_p} \qquad\qquad k_z = \frac{n}{R_p} \tag{2}$$

where m and n are integers, and a_p, R_p the plasma and torus radius, respectively. From the point of view of coupling, the plasma response is completely summarized in the surface impedance matrix $\underline{\underline{Z}}_p(k_y, k_z)$ [12]. Introducing the 'tangential' fields as

$$\vec{E}_t = E_y\, \vec{u}_y + E_z\, \vec{u}_z \qquad\qquad \vec{B}_t = -\vec{u}_z \times \vec{B}_o = B_z\, \vec{u}_y - B_y\, \vec{u}_z \tag{3}$$

(where $\vec{u}_\alpha$ are units vectors in the directions of the coordinates) the 2×2 symmetric matrix $\underline{\underline{Z}}_p$ is defined from the linear relation

$$\vec{E}_t(0) = \underline{\underline{Z}}_p \cdot \vec{B}_t(0) \tag{4}$$

satisfied at the plasma surface $x = 0$ by the causal solution of Maxwell's equations in the plasma. For each partial wave the surface impedance matrix $\underline{\underline{Z}}_p$ must be evaluated in principle by integrating the finite Larmor radius wave equations, either across the whole plasma, or at least until a position where the density is sufficiently large to impose outward radiation conditions exploiting the validity of the WKB approximation.

The upper limit to $n_\parallel = ck_z/\omega$ which can be efficiently coupled to the plasma is easily deduced from the dispersion relation of the compressional wave

$$n_\perp^2 = -\frac{(n_\parallel^2 - L)(n_\parallel^2 - R)}{(n_\parallel^2 - S)} \tag{5}$$

where R, L and $S = (R+L)/2$ are the elements of the cold plasma dielectric tensor [13]. Most heating scenarios (minority heating, cyclotron harmonic damping, electron heating and current drive) are optimized for modes with a sufficiently large $n_\parallel$, which are evanescent in vacuum and become propagative only above the cutoff $n_\parallel^2 = R$. The latter, therefore, must not be located too deeply inside the plasma. Recalling that $R = O(\omega_{pi}^2/\Omega_{ci}^2)$, it follows that the physics of heating requires to take into account partial waves up to values of the parallel index $n_\parallel = ck_z/\omega$ of the order of a fraction of $(m_i/m_e)^{1/2}$, essentially independently from the plasma size. Since the reactive part of the antenna impedence is influenced also by evanescent waves which are not radiated, however, the selfconsistent evaluation of the antenna characteristics typically requires to extend the exploration in k_z to values of the order of the inverse of the antenna width; the corresponding values of $n_\parallel$ are at least two or three times larger than those which contribute to the loading resistance. Similarly, only the few lowest values of $n_y = ck_y/\omega$ can be radiated efficiently into the plasma: since $n_x^2 = n_\perp^2 - n_y^2$, a finite k_y enhances the evanescence close to the antenna. For an accurate evaluation of the complex antenna impedance, however, it is necessary to explore a range of n_y^2 about as large as the range in n_z^2. The reason is that, although a fast-wave antenna is usually much longer in the y than wide in the z direction, its selfinductance is strongly influenced by contribution of feeders and shorts with evanescence length of the same order as the transverse width of the conductors [5].

According to Eqs. (2), on the other hand, the density of modes is inversely proportional to the plasma size in each of the two ignorable coordinates. From these elementary considerations we can conclude that the number of modes which must be taken into account increases as the square of the plasma dimensions, and, for a given plasma size, as the square of the frequency. It is clear, therefore, that for tokamaks of the size of JET or ITER a systematic frequency-dependent investigation of the electric properties of IC antennas can be a very heavy task. It should also be mentioned that obtaining $\underline{\underline{Z}}_p$ with good accuracy from the numerical integration of the wave equations in the plasma

becomes increasingly difficult for the Fourier modes with very short evanescence length required to evaluate the reactive part of the complex power.

To speed up antenna evaluations, in [14] we have derived analytic expressions for the surface impedance matrix of large plasmas, assuming that the WKB approximation can be used already at the edge of the plasma. For this purpose, the boundary conditions which connect the three independent solutions of the finite Larmor radius (FLR) wave equations in the plasma to the two solutions in vacuum has been established, and it has been shown that they guarantee the continuity of the total power flux entering the plasma. The values of $\underline{\underline{Z}}_p$ obtained analytically are in excellent agreement with numerical evaluations, provided that no singularity of the wave equations is present in the near-field region. This is not astonishing, since it amounts to a confirmation of the accuracy of the WKB approximation. The availability of relatively simple yet accurate analytic expressions for $\underline{\underline{Z}}_p$ makes possible a substantial reduction of the computing time required to calculate the properties if IC antennas.

It is often also useful to evaluate the electrical properties of antennas in vacuum: by comparing the results with the properties measured on a test bank or with estimations based on simple transmission line models of the antenna itself, one can test the accuracy of the numerical simulations. In addition, the plasma is likely to influence strongly the loading resistance of the antenna, but only weakly its reactive impedance, particularly in the presence of a Faraday screen. The behaviour of an antenna in vacuum or with a dummy load is therefore significant also for the plasma-loaded case: for example, the frequencies at which the antenna is resonant will be little affected by the plasma, although the quality factor of the resonances should appreciably decrease if coupling to the plasma is good.

These considerations have motivated us to produce a code which combines the antenna module of the FELICE code [15] with the fast evaluation of the plasma response based on the WKB theory. This code, which has been named ANTWKB, can evaluate also antennas radiating towards a vacuum half-space or on an absorber. Another advantage of an independent antenna package is that it does not need large arrays to store partial results, and is therefore less memory consuming and more flexible in the number of components which can be included in the Fourier representation of the fields.

The antenna routines of ANTWKB and FELICE are based on the formalism presented in [12] for the solution of Maxwell equations in vacuum. With respect to [12], however, a few changes and generalizations have been made:

a) The solution has been formulated in terms of impedances only, avoiding admittances. The two are perfectly equivalent in principle, but impedances are numerically more convenient, because they remain well-behaved also near perfect conductors.

b) The currents in feeders and shorts are no more assumed to be constant (since these conductors are in the same situation as the central conductor of a coaxial line, the same propagation constant as in vacuum is to be expected). We have found that taking into account propagation in the radial conductors is important at high frequencies.

c) The Ritz procedure has been extended to the case of several coupled antennas.

The third generalization, sketched in the Appendix, is the most important, since it allows in principle to evaluate selfconsistently the coupling constants of arrays. Implementing the general case, however, requires a major rearrangement of the code structure; for the moment, therefore, only the case of two loops fed in parallel by the same line has been implemented. The simplest example of such configurations is a T-antenna, which can be easily treated also as a single element by exploiting its symmetry. Having checked that the two approaches give the same results in this case, we have applied the new possibility to the violin antenna proposed for ITER [16], which is just an asymmetric T-antenna with two arms of very different lengths. Results for arrays will be presented separately when the necessary modifications to the code are ready.

The paper is organized as follows: sections 2 and 3 introduce the way in which different antennas are characterized in the ANTWKB code; sections 3 to 7 present applications to a number of cases of practical interest, both without and with plasma. Several antenna configurations are routinely available in ANTWKB:

1) A simple strap antenna fed at one end and shorted at the other;

2) A push-pull antenna with symmetric feeders at both ends and shorted in the middle;

3) The ASDEX Upgrade antenna (described below);

4) The violin antenna [16].

In cases 1) and 4) the antenna can be terminated on a capacitor instead than on a short. In addition, the code is so organized that it should be relatively easy for the user to add any additional configuration which might be of interest. Here we will present examples for cases 1), 3) and 4) in vacuum, and for case 1) and 4) with plasma. Some conclusions will be summarized in section 8.

2 – Input, radiation and effective resistance. The output of the ANTWKB code consists of the complex input and radiation (or loading) impedances of the antenna, and the spectral decomposition of the launced power. The latter is useful to estimate the power balance and the power deposition profiles in heating experiments; the input impedance Z_F, on the other hand, is the most important quantity characterizing the antenna behaviour. As well known, Z_F is the ratio of voltage to current at the entrance point of the antenna,

$$V_F = Z_F I_F \qquad\qquad Z_F = R_i + iX_i \tag{6}$$

Its knowledge is necessary and sufficient to treat the antenna as a passive element in the h.f. power line. The radiation impedance, on the other hand, is defined in terms of the complex power

$$P_{compl} = \frac{1}{2}\int \vec{E}_t^* \cdot \vec{J}_t \, d\ell = \frac{1}{2} Z_L |I_S|^2 \qquad\qquad Z_L = R_{rad} + iX_{rad} \tag{7}$$

where the integral extends over the antenna conductors, and I_S is the current in the short, which is normally also the peak current in the antenna (floating antennas tend to couple electrostatically to short wavelength surface waves in the plasma, and must be avoided in IC heating). Since the code neglects the internal resistance of the antenna, the real part of P_{compl} is the radiated power P; moreover

$$P = \frac{1}{2} R_{rad} |I_S|^2 = \frac{1}{2} R_i |I_F|^2 \tag{8}$$

Neither Z_F nor Z_L, however, are easily accessible experimentally, except on a test bank. During operation in ICRF experiments, it is instead customary to deduce from the measured launched power P an effective resistance R_{eff} defined as

$$P = \frac{1}{2} R_i |I_F|^2 = \frac{1}{2} R_{eff} |I_{max}|^2 = \frac{1}{2} R_{eff} \frac{V_{max}^2}{Z_{oc}^2} \tag{9}$$

where I_{max} and V_{max} are the peak voltage and peak current, respectively, in the coaxial line feeding the antenna, and Z_{oc} its characteristic impedance. In particular R_{eff} is directly related to the maximum power which can be transmitted, which is usally limited by the maximum voltage which the line can stand.

To obtain the relation between the input impedance Z_F of the antenna and the effective resistance R_{eff} measured experimentally, one can start from the solutions of the transmission-line equations in the coaxial,

$$\begin{aligned} V(s) &= V_F \left\{ \cos k_o s - i \frac{Z_{oc}}{Z_F} \sin k_o s \right\} \\ I(s) &= I_F \left\{ \cos k_o s + i \frac{Z_F}{Z_{oc}} \sin k_o s \right\} \end{aligned} \tag{10}$$

To evaluate I_{max}, we note that

$$\begin{aligned}\left|\frac{I(s)}{I_F}\right|^2 &= (\cos k_o s - z_i \sin k_o s)^2 + r_i^2 \sin^2 k_o s \\ &= \frac{1}{2}\Big\{ (r_i^2 + z_i^2 + 1) - (r_i^2 + z_i^2 - 1)\cos 2k_o s - 2z_i \sin 2k_o s \Big\}\end{aligned} \tag{11}$$

where

$$z_i = \frac{X_i}{Z_{oc}} \qquad\qquad r_i = \frac{R_i}{Z_{oc}} \tag{12}$$

and we have taken into account that Z_{oc} is purely real. The r.h. side of (11) is stationary where

$$\tan 2k_o s_M = \frac{2z_i}{r_i^2 + z_i^2 - 1} \tag{13}$$

Defining

$$A = \sqrt{(r_i^2 + z_i^2 - 1)^2 + 4z_i^2} \tag{14}$$

we can rewrite (11) as

$$\left|\frac{I(s)}{I_F}\right|^2 = \frac{1}{2}\Big\{ (r_i^2 + z_i^2 + 1) + A\cos 2k_o(s - s_M) \Big\} \tag{15}$$

the choice of sign being dictated by the requirement that $|I(s_M)|^2$ must be a maximum. From (9) then follows

$$R_{eff} = \frac{R_i}{f(r_i, z_i)} \tag{16}$$

with

$$f(r_i, z_i) = \frac{1}{2}\Big\{ (r_i^2 + z_i^2 + 1) + \sqrt{(r_i^2 + z_i^2 - 1)^2 + 4z_i^2} \Big\} \tag{17}$$

with r_i and z_i defined by (12). The behaviour of the function $1/f(r_i, z_i)$ is illustrated in fig. 1. Note that R_{eff} is always smaller than the input resistance R_i, and does not depend from the sign of the reactive part of the input impedance Z_i (whether 'inductive' or 'capacitive'). To evaluate R_{eff}, moreover, it is not necessary to know the radiation resistance R_{rad} of the antenna, as expected.

By construction, the running complex impedance $Z_c(s) = V(s)/I(s)$ in the coaxial is real at the point $s = s_M$. Hence the whole line beyond s_M, including the antenna, is equivalent to a purely resistive load R_{eff} inserted directly at s_M. From this remark it is not difficult to derive the alternative expression

$$R_{eff} = \frac{Z_{oc}}{S} \tag{18}$$

where S is the standing wave ratio in the coaxial,

$$S = \frac{1+|\Gamma|}{1-|\Gamma|} = \left(\frac{1+r_i^2+z_i^2+A}{1+r_i^2+z_i^2-A}\right)^{1/2} \tag{19}$$

Γ being the reflection coefficient, and the last expression being deduced from Eq. (15). From these equations it can be shown [17] that if the antenna is itself a transmission line with characteristic impedance Z_{oa}, and $R_{rad} \ll Z_{oa}$, R_{eff} is smaller or larger than R_{rad} depending on whether Z_{oc} is smaller or larger than Z_{oa}. Although this relation has no universal validity, it is a useful guideline in the choice of the coaxial impedance Z_{oc}.

3 – Representation of the antenna currents. For the implementation of the variational method it is necessary to have a reasonable representation of the current in the antenna. In the main conductors we assume a factorized distribution of the form

$$J_\eta^a(\eta,\zeta) = \frac{I_A}{w_a} f_a(\eta)\, g_a(\zeta) \tag{20}$$

where η and ζ are orthogonal coordinates along and across the conductors, respectively (for fast wave antennas usually $\eta = y$ and $\zeta = z$; the code, however, can take into account misalignment with respect to the static magnetic field due to the poloidal field of the tokamak). With the conventions

$$\mathrm{Max}_\eta \{|f_a|\} = 1 \qquad\qquad \int_A g_a(\zeta)\, d\zeta = w_a \tag{21}$$

I_A is the total peak current at the short, and the form factors f_a and g_a are dimensionless and of order unity. In all examples $g_a(\zeta)$ has been taken simply equal to unity, although profiles peaked towards the edges of the strips in the transverse direction have also been tested. The current in the radial conductors is then

$$J_x^a(\eta,\zeta) = \frac{I_A}{w_a} \sum_{\{F\}} \sigma_F\, \delta(\eta-\eta_F)\, f_a(\eta)\, g_a(\zeta)\, h_a(x) \tag{22}$$

where the sum extends to all feeders ($\sigma_F = +1$) and shorts ($\sigma_F = -1$). The function $h_a(x)$ takes into account radial propagation and has the form of a transmission line solution with boundary conditions at the wall and at the insertion point on the main conductor (the propagation constant in feeders and shorts is taken as given, i.e. it is not determined as part of the variational procedure).

To write $f_a(\eta)$ we have assimilated the antennas to one or several pieces of transmission line, taking into account the boundary conditions $dJ/d\eta = 0$ at shorts. Optionally,

ANTWKB can be asked to determine the value of the propagation constant ν_a which makes the variational functional stationary. This, however, has the disadvantage of assuming for practical reasons a real propagation constant, and therefore restricts excessively the class of test functions. Here, therefore, we use only the Ritz algorithm [11]-[12]. In this approach $f(\eta)$ is assumed to be the sum of several transmission-line functions with different values of ν_a

$$f_a(\eta) = \sum_{j=0}^{r} c_j f_a(\nu_a(j)\, k_o \eta) \tag{23}$$

($k_o = \omega/c$), and the variation determines the complex coefficients c_j. The values $\nu_a(j)$ are in principle arbitrary: the basis functions are not required to be orthogonal to each other, and the results are very robust to changes in the representation of $f_a(\eta)$. The best convergence, however, is obtained by chosing the $\nu_a(j)$ commensurate with the electrical length of the antenna,

$$\nu_a(j) = \frac{j\,\kappa}{k_o \ell_a} \qquad\qquad j = 0,\ 1, \ldots,\ r \tag{24}$$

and κ is a number of order unity. Including the constant distribution $j = 0$ is useful at low frequency ($k_o \ell_a \ll 1$), indifferent if the antenna is not electrically short. In the applications three ($j = 0$, 1 and 2) to five modes have been used, with $\kappa = 0.85$. It should be stressed that there is no point in including modes with $\nu_a(j)$ larger than the largest value of n_y used in the solution (1) of Maxwell's equations; $r = 3$ is a good compromise at all frequencies, ensuring an accuracy of the order of a few percent, except near antenna resonances where the error appears to increase to 10-20%.

By far the largest uncertanties in the results are due to the discretization of the Fourier expansion (1) for the electromagnetic field in vacuum and in the plasma, as it will become clear from the examples. In the applications we have used mostly 200 modes in the toroidal and 100 in the poloidal direction (2 10^4 Fourier components altogether), and occasionally up to 10 times more. Depending on the complexity of the antenna (number of conductors) each point in a frequency scan requires between 10 and 30 s on a Cray YMP for an antenna radiating in vacuum, and two to three times longer in the presence of plasma. The CPU time required by FELICE to integrate the wave equations over 1 m inside the plasma in order to obtain the surface impedance matrices for the same number of Fourier components would be several h. Although this is partly compensated by storing the tables of $\underline{\underline{Z}}_p$ so that they can be used for different antennas without running FELICE again, the advantage of the independent antenna package is obvious.

4 – Simple feeder-to-short antenna. The current distribution in a simple strap fed at $\eta = 0$ and terminated at $\eta = \ell_a$ treminated by a short or a capacitor (fig. 2) can be written (omitting for simplicity the summation of Eq. (23))

$$f_a(\eta) = \sigma_{\ell_a} \{\cos k_o \nu_a (\eta - \ell_a) + Q_a \sin k_o \nu_a (\eta - \ell_a)\} \tag{25}$$

where σ_{ℓ_a} is the sign of ℓ_a (orientation of the antenna), and Q_a is either zero (short) or a constant of order unity and negative.

Here we consider the shorted case with geometrical dimensions as summarized in Table 1; in order to have the simplest possible configuration, no Faraday screen was included. This antenna should behave as a piece of transmission line (TL) terminated on a short, except that its dimensions are such that it is not possible to predict accurately the distributed capacitance from the quasistatic approximation. The plots of the input resistance and impedance versus frequency confirm this expectation (fig. 3). From the position of the $\ell_a = \lambda/2$ resonance and the low-frequency behaviour of Z_i one can deduce a dimensionless propagation constant $\nu_a = 1.16$ and a characteristic impedance $Z_{oa} = 63.5$ Ohm (distributed capacity $C_a = 6.11\ 10^{-11}$ F/m, distributed inductance $L_a = 2.46\ 10^{-7}$ H/m). The equivalent TL characteristic impedance Z_a is obtained from the input impedance at a frequency f well below the resonance frequency $f_{\lambda/4}$ as

$$Z_{oa} = \frac{2}{\pi} \lim_{f \to 0} \frac{f_{\lambda/4}}{f} Z_i(f) \tag{26}$$

This relation should hold, according to the TL model, in the limit of an electrically short antenna, $\nu_a\, k_o \ell_a \ll 1$.

In this frequency scan we used 300 Fourier components in z and 100 in y, with a discretization corresponding to the dimensions of ITER, namely $R_p = 7.75$ m, $a_p = 4.50$ m (the latter being the vertical radius for an ellipticity of 1.6). The upper limits of n_z and n_y are then 73.9 and 42.6, respectively; the latter value allowed to include 5 modes in the Ritz representation of the currents. These values are largely sufficient for good convergence at all frequencies, so that we can be shure that the small amplitude irregularities in the numerical results with varying frequency are not due to bad numerics. The irregularities are particularly visible in the plots of the loading and effective resistance, fig. 3 c). As shown in fig. 4, by choosing a slightly different discretization of k_y and k_z, it is possible to run the frequency scan so that the results are smooth (although in this case, to do so while using the same number of Fourier components, we were obliged to accept a somewhat poorer convergence, and to use only three modes in the Ritz representation of the currents). Before explaining how this can be done, however, it is convenient to discuss first the results for a more complicated antenna with Faraday

screen, for which the oscillatory behaviour of R_{rad} with frequency is so marked that its origin becomes immediately clear.

Here we mention that with the values of the distributed constants estimated as above, and assuming losses such that $R_a/\omega C_a = 0.01\, f$ (Mhz), the transmission line predictions for Z_i and R_i, shown in fig. 5, agree not only qualitatively, but almost quantitatively with the results of ANTWKB (most of the discrepancy can be attributed to a poor modeling of the frequency dependence of the radiation losses in the TL approximation). If the characteristic impedance of the feeding coaxial is 60 Ohm, moreover, the radiation and effective resistances are nearly equal at all frequencies. According to the remark following Eq. (19), this confirms that this antenna is behaving as a segment of transmission line with a well-defined, frequency-independent, characteristic impedance of about 60 Ohm, as estimated above. In other words, the code reproduces well the expected behaviour of a shorted segment of transmission line.

This remains true if an ideal Farady screen is added, as shown in fig. 6. The intrinsic characteristics of the equivalent transmission line with screen are found to be $C_a = 1.32\ 10^{-10}$ F/m, $L_a = 2.67\ 10^{-7}$ H/m; the larger capacity increases the effective propagation constant to 1.79 and decreases the characteristic impedance to 45 Ohm. The radiation load in vacuum, moreover, is appreciably decreased by the screen.

5 – The ASDEX Upgrade antenna. We have next tested the code on the Asdex Upgrade antenna [18], shown schematically in Fig. 7. The dimensions of the two loops, summarized in Table 2, are such that they should have nearly the same inductance, and the folding of the conductors is such that, at least at low frequencies, a nearly uniform current should be presented to the plasma by the two outer conductors, as required for good coupling. We shall see that this property remains well satisfied even above the first antenna resonance.

If I_u^S and I_d^S are the currents in the upper and lower short, respectively, and defining

$$Q = \frac{I_d^S}{I_u^S} = \frac{I_d^F}{I_u^F} \frac{\cos \nu_u k_o (2L_u - y_F)}{\cos \nu_d k_o (L_d + y_F)} \tag{27}$$

the currents in each loop, with reference to fig. 7 can be written as follows:

a) Inner conductors:

$$f_1(y) = \begin{cases} -\cos \nu_u k_o (2L_u - y) & \text{if } y_F < y < L_u \\ Q \cos \nu_d k_o (L_d + y) & \text{if } 0 < y < y_F \end{cases} \tag{28}$$

b) Outer conductors:

$$f_2(y) = \begin{cases} \cos \nu_u k_o y & \text{if } 0 < y < L_u \\ Q \cos \nu_d k_o (L_d + y) & \text{if } -L_d < y < -g \end{cases} \tag{29}$$

A transmission-line model of this antenna is complicated, because the main and return conductors are in different situations, and must therefore be expected to have different characteristic constants. The results of ANTWKB, on the other hand, can be compared with accurate test bank measurements [19]. They show that the $\lambda/4$ resonance of the antenna lies at 42 Mhz, and, using Eq. (26), suggest an equivalent TL characteristic impedance at low frequency of about 18 Ohm. It should be stressed, however, that precise agreement is unlikely to be attained for several reasons. In the first place, in the real antenna, the distance between main and return conductor is variable, to accomodate the structure in the available space between separatrix and wall in the tokamak. Since the theory is available only for main conductors in planes parallel to the wall (and to the plasma surface), we were obliged to take an average value for this distance. Strictly speaking, moreover, the antenna consists of two loops fed in parallel; we have nevertheless treated it as a single element, assuming the two loops well balanced, so that the current from the feeder divides equally between the two arms, i.e. $Q = 1$ in Eqs. (28)-(29). This has been found to be nearly true on the test bench, in agreement with the design goal. In principle, as we shall see in the next section, ANTWKB could evaluate separately the current in each loop; to enter the necessary data for an antenna as complicated as this one, however, is rather cumbersome, and we have not attempted it. Finally, the test bench measurements have been made for two antennas of this kind parallel to each other and oriented in opposite directions, the same configuration as in the ASDEX Upgrade tokamak. Although the measurements allow conclusions also on the behaviour of each antenna separately, the comparison is necessarily indirect. We should also add that, since there are two shorts in which flows a different current, the definition of R_{rad} is not univoque. For simplicity, we have defined it using as reference the current in the middle-plane short. We recall that the effective resistance R_{eff}, by contrast, is always uniquely defined once the impedance of the coaxial line is given.

The complex input impedance obtained with ANTWKB by discretizing the spectra according to the Asdex Upgrade periodicity ($R_p = 1.67$ m, $a_p = 0.5$ m) is shown versus frequency in fig. 8. It is immediately clear that these results have nothing in common with the measured ones. The test bank, however, is in a large room, so that the very short periodicities of Asdex Upgrade are likely to be inappropriate for this simulation. We have therefore re-run the frequency scan putting the antenna in a larger square box with $R_p = a_p = 5$ m. The results, shown in fig. 9, begin to recall the measured ones,

but show, enhanced, the same kind of irregular behaviour already noted in the case of a simple antenna (fig. 3). This becomes particularly evident if we plot the effective resistance versus frequency (fig. 9 c). The transformation from R_i to R_{eff} eliminates the effects of the large $\lambda/4$ antenna resonance; the remaining periodic peaks in R_{eff} have nothing to do with the antenna itself, but appear precisely at those frequencies at which a new partial wave in the Fourier representation (1) changes from evanescent ($n_y^2 + n_z^2 > 1$) to propagative ($n_y^2 + n_z^2 < 1$). The reason why these parasitic resonances are stronger in this case than in the previous one is that the idealized Faraday screen helps guiding waves with $n_x = 0$ along the poloidal and toroidal directions; the artificially imposed periodicity makes them interact again and again with the antenna. The results of fig. 8 are dominated by "box resonances" of this kind.

These consideration also suggest a way of eliminating the parasitic resonances, namely by chosing the dimension of the toroidal box to be frequency dependent in such a way as to be always at the mid-point between two peaks. For a square box the recipee is

$$R_p = a_p = \left(N_p + \frac{1}{2}\right) \frac{c}{2\pi f} \tag{30}$$

where N_p is an integer which denotes the number of propagative modes with $0 \leq n_z < 1$ and $n_y = 0$, or with $0 \leq n_y < 1$ and $n_z = 0$. This way of discretizing the spectrum has also the advantage of making convergence robust and roughly frequency-independent. Since there are only about $4\,N_p^2$ propagative partial waves, where N_p is necessarily much smaller than the total number of components (in practice, we have used $N_p = 5$), it is clear that the sampling of radiating modes is rather poor. The accuracy obtained is nevertheless acceptable, since the normalization of the Fourier transform automatically compensates in part for the rough discretization.

The results obtained using the "variable box" normalization are shown in fig. 10 in vacuum and with a strong absorber. They are qualitatively quite similar to the experimental ones, although the $\lambda/4$ resonance is about 6 Mhz too high, and the values of the input impedance Z_i somewhat too small. Also, to reproduce the broad peak in R_{eff} with absorber around 50 Mhz we must use a coaxial line of 50 Ohm according to ANTWKB (fig. 11), while experimentally it appears already at 30 Ohm. As mentioned above, however, it would not be too difficult to improve agreement by changing slightly the radial distances between conductors and wall, and particularly the position of the Faraday screen.

In the case of the ASDEX Upgrade antenna it is particularly instructive to have a look to the selfconsistent current distribution predicted by the Ritz algorithm. At low frequencies the current in the the outer conductors is nearly uniform, as expected. This configuration is very robust: when the the ratio I_S/I_F increases as the frequency

approaches the $\lambda/4$ resonance, most of the variation takes place in the return conductors close to the walls (fig. 12 a). Above the resonant frequency (fig. 12 b) the current changes sign between feeder and shorts, but again the node occurs close to the feeder in the return conductors, so that the current in the outer conductors has the opposite direction, but is again quite homogeneous. The transition from one configuration to the other occurs rather abruptly around the resonant frequency. It is not difficult to understand the reason for this behaviour: the return conductors, being close to the metallic wall, are equivalent to segments of TL with higher capacity, hence larger propagation constant, and can therefore easily accomodate most of the variation of $J(\eta)$. This has the advantage that the antenna presents to the plasma a satisfactorily uniform current at most frequencies, as required for good coupling, which moreover corresponds always to the section closest to the shorts, which radiates best.

We conclude this section by mentioning that the variable box discretization of the spectrum can be used with advantage also in the presence of plasma, preferentially with different values of N_p in the toroidal and poloidal directions, chosen so that the effective values of a_p and R_p are as close as possible to the real ones. When the plasma is sufficiently absorptive, the suppression of spurious surface modes is more important than an exact sampling of the spectrum.

6 – Violin antenna. Recently [16] an antenna of new design has been proposed for ITER, and discussed using both a transmission-line model and numerical simulations. It is an asymmetric shorted T-antenna, with the feeder much closer to one end (fig. 13); the long arm should be the main radiating part, while the short arm should act as 'tuning' element. This launching structure, which has been appropriately named 'violin' antenna, has advantages from the point of view of its mechanical support, and should have an acceptable loading over a wide frequency band.

In each arm of the violin antenna the current distribution can be represented by a function of the form (25); in contrast to the case of the Asdex Upgrade antenna, however, it is obviously not possible to assume that the feeder current divides equally between the two arms. To determine the antenna current selfconsistently, therefore, the extension of the variational method to the case of two coupled loops is essential. In the quasistatic limit one would predict that the current in the short arm, which presents to the feeder a much lower impedance, should be about ten times larger than in the main arm; this is confirmed by the variational method at frequencies below about 15 Mhz. Near antenna resonances, on the other hand, the current in the two arms becomes comparable, and a non-negligible current in quadrature with the feeder can flow between the two shorts, ignoring the feeder. These current modes are 'natural

vibrations' of the antenna not unlike the vibrations of a violin string; formally, their excitation means that the coefficients of the Ritz superposition (23) can have a large imaginary part.

The physical dimensions of the violin antenna proposed for ITER in [16] are summarized in Table 3. The behaviour predicted by ANTWKB for this antenna radiating towards a vacuum half-space is presented in fig. 14 for two values of the distance between the conductor and the Faraday screen (the very tight screen distance of 1 cm was chosen to see how low the first antenna resonance could be made; in the following we will concentrate on the more realistic distance of 5 cm). It is instructive to compare these results with the predictions of a TL model of the antenna. Since the two arms are geometricall identical except for their length, and are fed in parallel, the input impedance seen by the coaxial line should be

$$Z_i = -Z_c \left\{ \cot \nu_a k_o \ell_1 + \cot \nu_a k_o \ell_2 \right\}^{-1} \tag{31}$$

where the effective characteristic impedance Z_c can be obtained from Eq. (26) using the effective length $L_{eff} = \ell_1 \ell_2 / (\ell_1 + \ell_2)$. When $\ell_2 \ll \ell_1$ the presence of the short arm shifts the first zero of the expression in bracketts in such a way that the first two antenna resonances should be roughly equispaced in frequency. This prediction of the TL model, however, is not completely confirmed by the numerical results. The ratio between first and second resonant frequency is found to be about 2.5, definitely less than the value 3 for a single line, but still larger than the approximate value 2 predicted by Eq. (31). As shown in fig. 15, therefore, the TL model can interpolate reasonably well either the first or the second resonance, but not both; it is also more difficult than in the case of a simple antenna to make a guess about the distributed losses which describes well both the height and the width of the two peaks of R_i. We attribute these discrepancies to the fact that the simple TL model (31) neglects the mutual coupling of the two loops, which is automatically taken into account by the variational method.

It is natural in this case to define the radiation resistance with reference to the current in the short of the major arm. In the absence of losses this current vanishes at a frequency just above each antenna resonance, so that when radiation losses are taken into account R_{rad} has large and broad peaks above the $\lambda/4$ resonance (fig. 16 a). This suggests that in vacuum this antenna is a good radiator over a broad frequency range. It should be noted, however, that the absolute values reached by R_{rad} are largely a matter of definition. The peaks of R_{rad}, moreover, can be completely suppressed by the transformation to R_{eff}, unless the impedance of the coaxial line is sufficiently large (fig. 16).

It is therefore important to investigate how efficient the violin antenna is in the presence of plasma. Figure 17 shows the results obtained with ANTWKB with a ITER-like pure deuterium plasma as load. The parameters chosen for these runs are summarized in table 4; note that only edge values are given, since the assumption that the WKB approximation can be used to evaluate the plasma surface impedance matrix makes all other parameters irrelevant. We have not made shure that this assumption is justified over the whole frequency range: on the contrary, it is likely to be invalid at frequencies around 34 and 68 Mhz, when the fundamental and first harmonic cyclotron resonance of deuterium, respectively, cross the outer plasma edge. We stress, however, that the load evaluated by ANTWKB is physically meaningful even in these frequency ranges, although it will differ somewhat from the real plasma load in the inhomogeneous tokamak configuration. It is also important to realize that in the presence of plasma, when the procedure mentioned at the end of section 5 is used to discretize the spectrum, the number of Fourier components required for convergence increases as the square of the frequency; at 80 Mhz we had to include 2.2 10^5 components (10^3 in the toroidal and 220 in the poloidal directions). Failing to use a systematic discretization of the spectrum and to ensure convergence results in spurious resonances and in discontinuities even stronger than in the vacuum case, which make any interpretation of the results impossible.

It is immediately apparent that the response of the violin antenna in the presence of plasma is qualitatively the same as in vacuum: the resonance frequencies are practically unchanged, X_i is reduced by a factor between 1.5 and 2, the effect being larger at low frequencies, and the quality of the antenna resonances is not significantly reduced by the plasma load. The radiation resistance above the first antenna resonance is again quite large, with peaks (not shown in fig. 17 b) of about 140 Ohm. It must be recalled, however, that R_{rad} does not characterize well the coupling efficiency of this antenna. As shown in fig. 18, at frequencies above the $\lambda/4$ resonance the current in the main short, although a local maximum, is by no means the largest current in the antenna. If the latter were used to define R_{rad}, its values would be reduced by more than an order of magnitude. Similarly, the two peaks of R_{eff} close to the antenna resonances are quite comfortable, but elsewhere the values of R_{eff}, although somewhat larger than in the vacuum case, remain rather low, implying a relatively large standing wave ratio and large voltages in the coaxial.

For comparison, fig. 19 shows a frequency scan in the presence of the same plasma for the simple feeder-to-short antenna of section 4 (with Faraday screen). While the input impedance is again little affected, the loading in the presence of plasma is considerably increased at low frequencies, and decreases again to values comparable or lower than in vacuum at frequencies above 50 Mhz. In spite of the fact that the total length of this antenna is only half that of the violin antenna, the effective resistance seen by a 50 Ohm

coaxial line is larger at all frequencies except in the vicinity of resonances of the latter. Incidentally, figs. 17 c and 19 c are a good warning against using the absolute values of R_{rad} to compare the launching efficiency of antennas of different design.

Although neither antenna has been optimized, the conclusion which can be drawn from this comparison is that the violin antenna is really superior only if used in the vicinity of its resonances (that it should be used above the $\lambda/4$ resonance was stressed in [16]). We believe that the poor performances at low frequencies are due to the fact that the violin antenna presents to the plasma a current with a dicontinuity in the poloidal direction at the position of the feeder. The Fourier spectrum of such a configuration is rich in large n_y components, which are poorly coupled to the plasma. This becomes less important near antenna resonances, where there is a large current component in quadrature with the excitation which is continuous at the feeders, as in the case of fig. 18. Elsewhere, however, the violin antenna is at disadvantage compared to an antenna of similar size but without discontinuity. If the radiation and effective resistances are evaluated with ANTWKB without making use of the variational method, but assuming instead a transmission line current distribution (with the propagation constant appropriate to locate the antenna resonances correctly, but at a frequency far from resonance), the values obtained for the long arm alone are typically an order of magnitude larger than for the complete violin antenna.

7 – Capacitively terminated antennas. The situation might be different, however, if the main conductor terminates on a variable capacity, which can be adjusted to match the antenna to the feeder line and to improve the effective resistance. This technique has been implemented in the TORE SUPRA IC antenne [20]. To investigate this case, we note that a capacity C_S at the end of a transmission line with distributed capacity C_a and propagation constant ν_a would give

$$Q_a = -\frac{C_a}{k_o \nu_a C_S} \tag{32}$$

in equation (25) (note that the current distribution (25) remains regular also in the limit $\nu_a \to 0$). Since (32) is the continuity of charge at the capacitor, it follows that the physically meaningful quantity is $Q = Q_a \nu_a$, which must therefore be the same for all current modes used in the Ritz algorithm. At a given frequency, on the other hand, we can made a scan over Q to determine the value which optimizes the launcing efficiency; this procedure is analogous to the experimental tuning of the capacity.

For our present example we have chosen the frequency of 45 Mhz, where the effective resistance of the shorted violin antenna is close to its minimum. The results are shown

in fig. 20 for the violin antenna, and in fig. 21 for the simple antenna of section 4 with Faraday screen. As expected from the TL model, there is a value of the variable capacity around $Q = 1$ which makes the antennas resonant, although the resonance is appreciably less marked than in a frequency scan. The responses of the two antennas to variations of Q are actually quite similar, except that their radiation resistances behave symmetrically with respect to the resonant Q value. In both cases the effective resistance has a clear peak on the side of the resonance on which the antenna as a whole begins to behave as a shorted transmission line. If allowance is made for the different lengths of the two antennas, moreover, the peak values of R_{eff} are essentially similar. It seems fair to conclude that terminating the conductor on a adjustable capacity is a more flexible method than the violin design to improve the radiation efficiency of the antenna over a broad range of frequencies. One should bear in mind, however, that a capacitively terminated strap is mechanically delicate and can hardly be realized without insulating elements relatively close to the plasma; the violin antenna, by contrast, is particularly robust and easily compatible with the reactor environnement.

8 – Conclusions. The code ANTWKB reproduces with reasonable accuracy the behaviour of simple IC antennas, and can be useful to investigate more complicated configurations. The code confirms the favorable features of the folded ASDEX Upgrade IC antenna, whose outer conductors present to the plasma a relatively uniform current at all frequencies in a broad domain, which, moreover, tends to be larger than in the return conductors. In the case of simple strap antennas, replacing the short by an adjustable capacity has been found to be a good way of improving the launching efficiency. The advantages of the 'violin' antenna [16], on the other hand, have been found to be restricted to the vicinity of the antenna resonance. Extensions of ANTWKB to deal with arrays of independently fed antennas, with individual conductors recessed in the wall or separated from each other by metallic septs would be desirable, and are partly in progress.

Extensive use of the code has shown the importance of using a suitable systematic discretization of the Fourier spectrum of the launced fields, and of including a sufficiently large number of Fourier components to ensure convergence in both the poloidal and toroidal directions. The semi-analytic evaluation of the surface impedance matrix of the plasma developed in [14] was essential to reach the latter goal with a reasonable numerical effort.

Aknowledgments. We are greatly indebted to Dr. J.M. Noterdaeme for many discussions and useful suggestions. We would also thank Dr. R. Koch, who has proposed several examples for the comparison and validation of available antenna codes within the ITER community which have been very useful for testing and improving ANTWKB.

Appendix – Variational formulation for coupled loops. To deal with antennas arrays the approach of Ref. [12] must be generalised to take into account the mutual interactions between different loops. For this purpose we consider the linear relation between voltage and current at the feeder point of each conductor,

$$V_q/d_q = \sum_p Z_{qp} I_p \qquad (A1)$$

where indexes p, q have been introduced to distinguish the conductors. The matrix Z_{qp} is symmetric, and has therefore generally $N_c(N_c+1)/2$ independent elements, where N_c is the number of conductors. As a consequence of (A1), the externally excited field at the feeder $\vec{r}_q$ can be written

$$\vec{E}_q^{ext}(\vec{r}_q) = -\sum_p Z_{qp}\, \underline{\underline{\mathcal{M}}}_{qp} \cdot \vec{J}_p(\vec{r}_q) \qquad (A2)$$

If conductor p is at distance w_p from the wall and $\Theta_{F_p}(y_p, z_p)$ is a step function which is unity at the p–th feeder and zero elsewhere, the linear operator $\underline{\underline{\mathcal{M}}}_{qp}$ is of the form

$$\underline{\underline{\mathcal{M}}}_{qp} \cdot \vec{J}_p(\vec{r}_q) = -\delta(x - w_q)\Theta_{F_q}(y_q, z_q) \int_{A_p} J_{p,x}(w_p, y_p, z_p)\Theta_{F_p}(y_p, z_p)\, dy_p\, dz_p \qquad (A3)$$

On the other hand the response of the system (including the load) induces at $\vec{r}_q$ an electric field which is a linear function of the currents in all conductors,

$$\vec{E}_q^{ind}(\vec{r}_q) = \underline{\underline{\mathcal{R}}}_{qp} \cdot \vec{J}_p \qquad (A4)$$

To obtain $\underline{\underline{\mathcal{R}}}_{qp}$ we use the Fourier representation of currents and fields, Eq. (1). Let

$$\vec{E}_p(n_y, n_z, x_q) = \underline{\underline{R}}_{pq}(n_y, n_z) \cdot \vec{J}_p(n_y, n_z, x_p) \qquad (A5)$$

be the field induced in the plane of conductor q by a Fourier component of the current flowing in the p–th conductor, all other conductors being passive. Then

$$\vec{E}_q^{ind}(\vec{r}_q) = \frac{1}{4\pi^2 R_p a_p} \sum_{n_y} \sum_{n_z} e^{i(n_y y_q + n_z z_q)}\, \underline{\underline{R}}_{qp}(n_y, n_z) \cdot \int_{A_p} \vec{J}_p^a(\vec{r}_p)\, e^{-i(n_y y_p + n_z z_p)}\, d\vec{r}_p \qquad (A6)$$

where R_p, a_p are the torus and plasma radius, respectively. Using this equation $\underline{\underline{\mathcal{R}}}_{qp}$ can be constructed by solving the wave equations in the plasma.

We must impose

$$\vec{E}_q^{ext}(\vec{r}_q) = \vec{E}_q^{ind}(\vec{r}_q) \tag{A7}$$

for each q and each choice of the excitation. Since the voltage applied to each conductor can be chosen independently, there are $N_c(N_c+1)/2$ such conditions, as required to determine the impedance matrix Z_{qp}. For this purpose, we multiply (A6) with currents $\vec{K}_q^a(\vec{r}_q)$ flowing in the q–th conductor, integrate over all conductors, and sum over q, we obtain in a few elementary steps

$$\begin{aligned} V &= \sum_q \sum_p K_q^* Z_{qp} I_p \\ &= 4\pi^2 R_o a \sum_q \sum_p \sum_{n_y} \sum_{n_z} \vec{K}_q^*(n_y, n_z) \cdot \underline{\underline{R}}_{qp}(n_y, n_z) \cdot \vec{J}_p(n_y, n_z) \end{aligned} \tag{A8}$$

A set of independent equations of the form (A7) is obtained by varying $\vec{K}_q^*(\vec{r}_q)$ while keeping K_q^* and one of the total currents I_p in turn constant, and all others equal to zero (by symmetry, only one of the two equations obtained by interchanging q and p needs to be retained). Thus the expression on the r.h. side of (A8) is the appropriate generalisation of the variational functional of [12]. Moreover, interchanging the role of the test and actual currents, and using easily proved symmetries of $\underline{\underline{R}}_{pq}$, it is possible to show that Z_{qp} will be symmetric as required. These results can be summarised by stating that the selfconsistent current distribution minimises all self and mutual energies, as one would expect.

To implement the variational principle with the Ritz method [12] we represent the currents in the conductors as

$$\vec{J}_p = I_p \sum_k \alpha_k^p f_k^p(y,z)\, \vec{u}_p \qquad \vec{K}_p^* = K_p^* \sum_k \beta_k^p f_k^p(y,z)\, \vec{u}_p \tag{A9}$$

where $\vec{u}_p$ is a unit vector along the p-th conductor, and other notations are standard. In this representation the variational sum is

$$V = \sum_q \sum_p K_q^* Z_{qp} I_p = \sum_q \sum_p \sum_j \sum_k K_q^* \beta_j^q R_{jk}^{qp} I_p \alpha_k^p \tag{A10}$$

with

$$R_{jk}^{qp} = 4\pi^2 R_o a \sum_{n_y} \sum_{n_z} f_j^q(n_y, n_z) \left(\vec{u}_q \cdot \underline{\underline{R}}_{qp}(n_y, n_z) \cdot \vec{u}_p \right) f_k^p(n_y, n_z) \tag{A11}$$

In practice, we must proceed differently in the case of independenly feeded loops (array antennas) and in the case of a T–antenna in which the same feeder excites two loops in parallel.

a) Independent loops. If all conductors are feeded independently, we must impose the additional conditions

$$\sum_k \alpha_k^p \bar{f}_k^p = 1 \qquad\qquad \sum_j \beta_j^q \bar{f}_j^q = 1 \tag{A12}$$

for each 'active' conductor p (q), where $\bar{f}_k^p$ are the values of the basis functions at the feeder position in each conductor. Variation with respect to β_j^q with $I_p = 1$ (or with respect to α_k^p with $K_q^* = 1$) in turn, and all other currents zero therefore gives

$$\lambda_{qp} \bar{f}_j^q = \sum_k R_{jk}^{qp} \alpha_k^p \qquad\qquad \lambda_{pq}^* \bar{f}_k^p = \sum_j \beta_j^q R_{jk}^{qp} \tag{A13}$$

where λ_{qp} are Lagrange multipliers for the conditions (A12). These can be inverted as

$$\alpha_k^p = \lambda_{pq} \sum_j \bar{f}_j^q (R_{jk}^{qp})^{-1} \qquad\qquad \beta_j^q = \lambda_{qp}^* \sum_k (R_{jk}^{qp})^{-1} \bar{f}_k^p \tag{A14}$$

(the inversion is with respect to the indexes j, k only). Finally, substitutiting into (A10)

$$\lambda_{pq} = \lambda_{pq}^* = Z_{pq} = \left\{ \sum_j \sum_k \bar{f}_j^q (R_{jk}^{qp})^{-1} \bar{f}_k^p \right\}^{-1} \tag{A15}$$

This is the required generalization of the results obtained in [12] for a single conductor.

b) T-antennas. In the case of a T-antenna we must take into account that the two loops are not feeded independently. With obvious notations, we can write

$$\begin{aligned} \vec{J}_1 &= \vec{u}_\eta \, I_o \, \xi \sum_k \alpha_k^1 f_k^1(y,z) \\ \vec{J}_2 &= -\vec{u}_\eta \, I_o (1-\xi) \sum_k \alpha_k^2 f_k^2(y,z) \end{aligned} \tag{A16}$$

and similarly for the conjugate K-currents. The coefficients α_k^p and β_j^q must satisfy (A12) as before. Variation with respect to α_k^p and β_j^q and ξ in this form, however, would lead to non–linear equations. Moreover, in this case, we are interested only in the input impedance Z_i of the antenna as a whole, rather than on the separate constants of the two half loops and their mutual impedance. It is therefore more convenient to treat the T-antenna as a single element by defining

$$\bar{\alpha}_k^p = \xi \, \alpha_k^p \qquad\qquad \bar{\beta}_j^q = (1-\xi) \beta_j^q \tag{A17}$$

which must now satisfy

$$\sum_k \left(\bar{\alpha}_k^1 \bar{f}_k^1 + \bar{\alpha}_k^2 \bar{f}_k^2\right) = 1 \qquad \sum_j \left(\bar{\beta}_b^1 \bar{f}_b^1 + \bar{\beta}_b^2 \bar{f}_b^2\right) = 1 \tag{A18}$$

The variation now give

$$\begin{aligned} \lambda \hat{f}_j^1 &= \sum_k \left(R_{jk}^{11} \hat{\alpha}_k^1 + R_{jk}^{12} \hat{\alpha}_k^2\right) \\ \lambda \hat{f}_j^2 &= \sum_k \left(R_{jk}^{21} \hat{\alpha}_k^1 + R_{jk}^{22} \hat{\alpha}_k^2\right) \end{aligned} \tag{A19}$$

which can be inverted as

$$\hat{\alpha}_k^p = \lambda \sum_q \sum_j \hat{f}_j^q \left(R_{jk}^{qp}\right)^{-1} \tag{A20}$$

(here the inversion must be done with respect to both set of indexes, which is immediate by considering $\{\alpha_k^1,\ \alpha_k^2\}$ as the components of a single vector). Then finally

$$\lambda = Z = \left\{ \sum_j \sum_k \bar{f}_j^q \left(R_{jk}^{qp}\right)^{-1} \bar{f}_k^p \right\}^{-1} \tag{A21}$$

which is differs from (A15) only by the meaning of the inverse matrix.

References.

[1] Adam J., Chauffage cyclotronique: impedance d' antenne en presence d' un mechanisme de forte absorption. Report EUR-CEA-FC 1004, 1979.

[2] Weynants R.R., Messiaen A.M., Leblud C., Vandenplas P.E., Proc. 2d Int. Symp. on Heating in Toroidal Plasmas, Como 1980, EUR-7424-EN, Vol. 1, p. 487.

[3] Messiaen A.M., Koch R., Bhatnagar V.P., Evrard M., Luwel P.E., Vandenplas E.P., Weynants R.R., Proc. 3d Grenoble–Varenna Int. Symp. on Heating in Toroidal Plasmas, Grenoble 1982, EUR-7979-EN Vol. 1, p. 243.

[4] Messiaen A.M., Evrard M.P., Koch R., Lamalle Ph., Vandenplas E.P., Weynants R.R., Proc 4th Int. Symp. on Heating in Toroidal Plasmas, Roma 1984, Vol. 1 p. 303.

[5] V.P. Bhatnagar, R. Koch, A.M. Messiaen, R.R. Weynants, Nucl. Fus. **22** (1982) 279.

[6] Vdovin V.L., Nucl. Fus. **23** (1983) 1435.

[7] Ram A., Bers A., Nucl. Fus. **24** (1984) 679.

[8] Lehrman I.S., Colestock P.L., IEEE Trans. Plasma Sci. **PS–15** (1987) 285.

[9] Brambilla M. Nucl. Fus. **28** (1988) 549.

[10] Chiu S.C., Mayberry M.J., Bard W.D., Nucl. Fus. **30** (1990) 2551.

[11] Teilhaber, K., Jacquinot J., Nucl. Fus. **24** (1984) 541.

[12] Brambilla M., Plasma Phys. Contr. Fus. **35** (1993) 41.

[13] Stix T.H. *Waves in plasmas.* American Institute of Physics (N.Y.) 1993.

[14] Brambilla M., Nucl. Fus. **35** to be published.

[15] Brambilla M., Plasma Phys. Contr. Fus. **31** (1989) 723.

[16] Bhatnagar V.P., Jacquinot J., Nucl. Fus. **34** (1994) 886.

[17] Noterdaeme J.M., private communication.

[18] Noterdaeme J.M. et Al., Fus. Eng. Des. **24** (1994) 65.

[19] OakRidge RF group, private communication.

[20] Beaumont B., Agarici G., Kuus H., 15th Symposium on Fusion Technology (Utrecht 1988), North-Holland 1989, Vol. 1 p. 503.

Figure captions.

Fig. 1 – The factor $1/f(r,z)$ in the transformation between the input and effective resistance (Eq. (17)).

Fig. 2 – Simple feeder-to-short antenna.

Fig. 3 – Characteristics of a feeder-to-short antenna without Faraday screen (dimensions as in Table 1, spectral discretization according to ITER periodicity): a) - b) resistive and reactive part of the input impedance; c) radiation and effective resistance.

Fig. 4 – Comparison of the results of ANTWKB for the feeder-to-short antenna with the predictions of the transmission-line model ($C_a = 6.11\ 10^{-11}$ F/m, $L_a = 2.46\ 10^{-7}$ H/m).

Fig. 5 – Same as fig. 3, but with spectral discretization according to Eq. (30) with $N_p = 5$.

Fig. 6 – Same as fig. 5, with Faraday screen.

Fig. 7 – Idealized model of the ASDEX Upgrade IC antenna.

Fig. 8 – Characteristics of the ASDEX Upgrade IC antenna; spectral discretization according to the periodicity of the ASDEX Upgrade tokamak.

Fig. 9 – Characteristics of the ASDEX Upgrade IC antenna; spectral discretization in a square box of 5×5 m.

Fig. 10 –Characteristics of the ASDEX Upgrade IC antenna; spectral discretization according to Eq. (30) with $N_p = 5$.

Fig. 11 – Comparison of the effective resistance of the ASDEX Upgrade IC antenna in vacuum and with a resistive load (a very resistive wall at 5 cm from the Faraday screen).

Fig. 12 – Current distribution in the ASDEX Upgrade IC antenna at 40 and 60 Mhz (below and above the $\lambda/4$ resonance, respectively). The current in the feeder is unity. The heavier lines are the currents in the outer conductors; for convenience, the currents in the inner conductors are represented with changed sign.

Fig. 13 – The "violin" antenna.

Fig. 14 – Input impedance of the violin antenna radiating in vacuum. Spectral discretization according to Eq. (30) with $N_p = 4$.

Fig. 15 – Comparison of the results of fig. 14 with the transmission line model of the violin antenna. Dots: numerical values; dashed lines: characteristics of the TL chosen

to match the first resonance; full lines: characteristics of the TL chosen to match the second resonance.

Fig. 16 – Radiation and effective resistance of the violin antenna in vacuum (the peak of R_{rad} at 45 Mhz exceeds 250 Ohm).

Fig. 17 – Characteristics of the volin antenna in the presence of a Deuterium plasma (plasma parameters as in Table 4; the peak of R_{rad} at 45 Mhz exceeds 150 Ohm).

Fig. 18 – Current distribution in the violin antenna (with plasma) at 68.5 Mhz. The current in the feeder is unity. The dotted line is the current in quadrature with the feeder excitation, which is continuous at the feeder.

Fig. 19 – Characteristics of the feeder-to-short antenna in the presence of a Deuterium plasma (plasma parameters as in Table 4).

Fig. 20 – Characteristics of the violin antenna (with plasma) at 45 Mhz, assuming that the main arm is terminated on a varying capacity.

Fig. 21 – Characteristics of the feeder-to-short antenna (with plasma) terminated on a varying capacity, at 45 Mhz.

TABLE 1
Simple feeder-to-short antenna

Length of the main strap	1.5	m
Width	0.25	m
Distance from the wall	0.32	m
Distance conductor-Faraday screen	0.05	m

TABLE 2
Asdex Upgrade antenna

a) Outer conductors		
Length of the upper arm	0.54	m
Length of the lower arm	0.34	m
Distance from the wall	0.10	m
Distance from the Faraday screen	0.025	m
Gap between upper and lower arm	0.045	m
Width	0.18	m
b) Inner conductors		
Distance from the wall	0.01	m
Position of the feeder	+ 0.32	m
Width	0.18	m

TABLE 3
Violin antenna

Major arm length	2.6	m
Minor arm length	0.4	m
Width	0.25	m
Distance from the wall	0.32	m
Distance form Faraday screen	0.05	m

TABLE 4
Plasma parameters

Plasma composition:	pure D^+
Major radius	7.75 m
Minor radius	2.80 m
Vertical plasma dimensions (k_y)	3.70 m
Magnetic field at outer edge	4.475 T
Edge electron density	$0.8\ 10^{20}$ m^{-3}
Edge temperature	50 eV

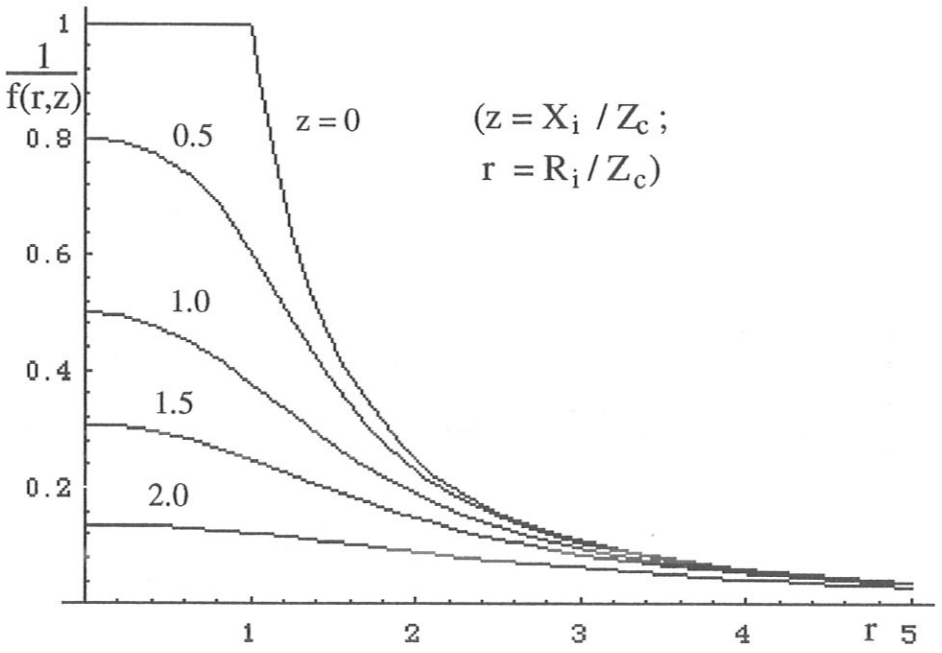

(Fig. 1)

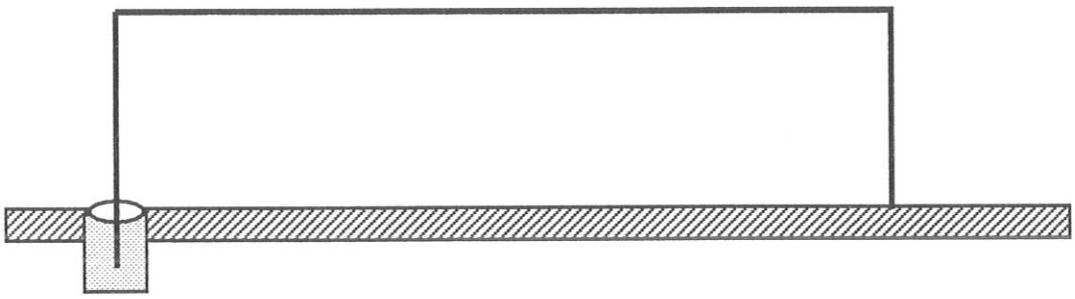

(Fig. 2)

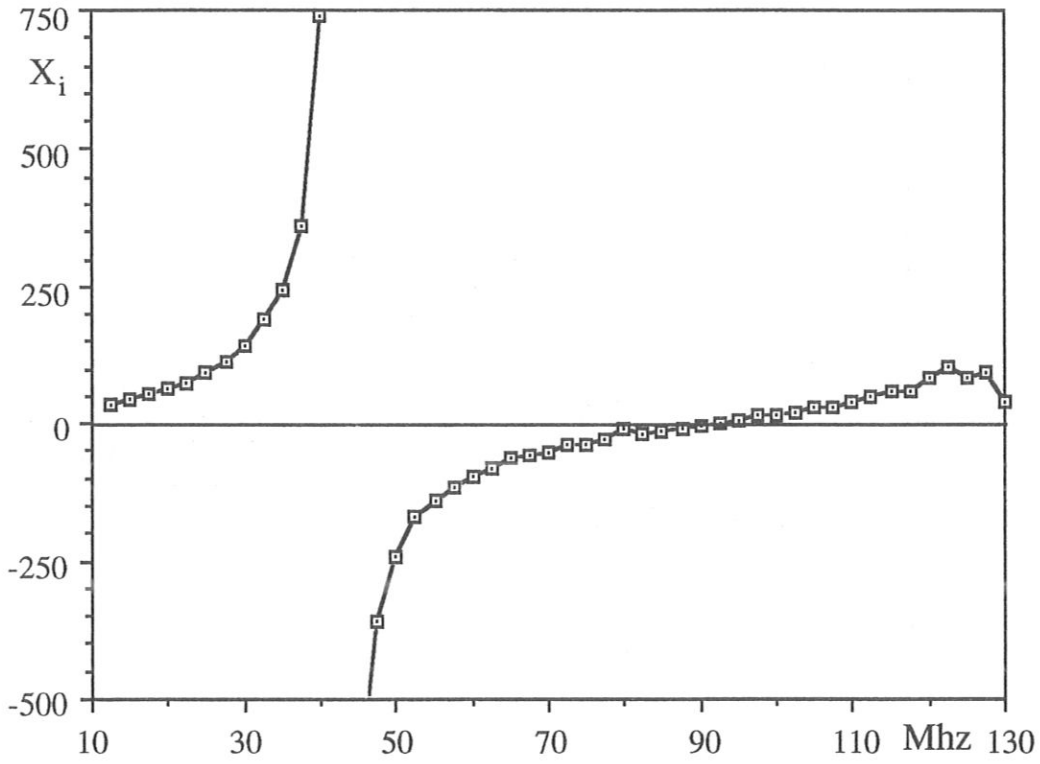
750
X_i
500
250
0
-250
-500
10
30
50
70
90
110
Mhz
130

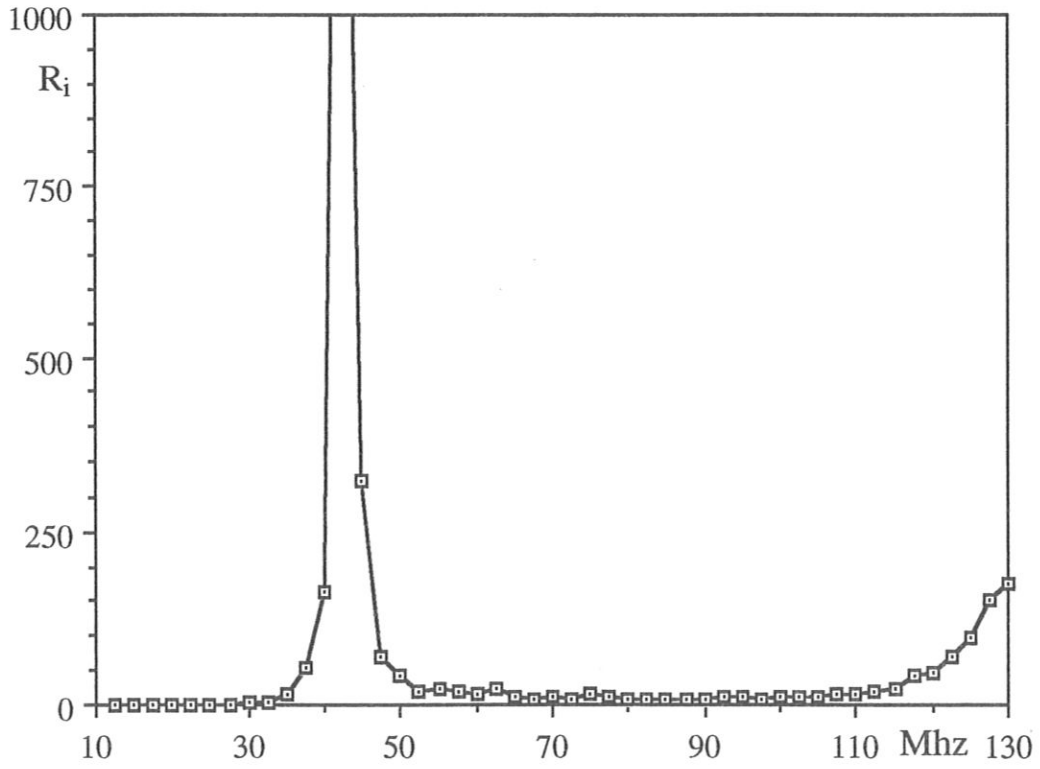
1000
R_i
750
500
250
0
10
30
50
70
90
110
Mhz
130

(Fig.3)

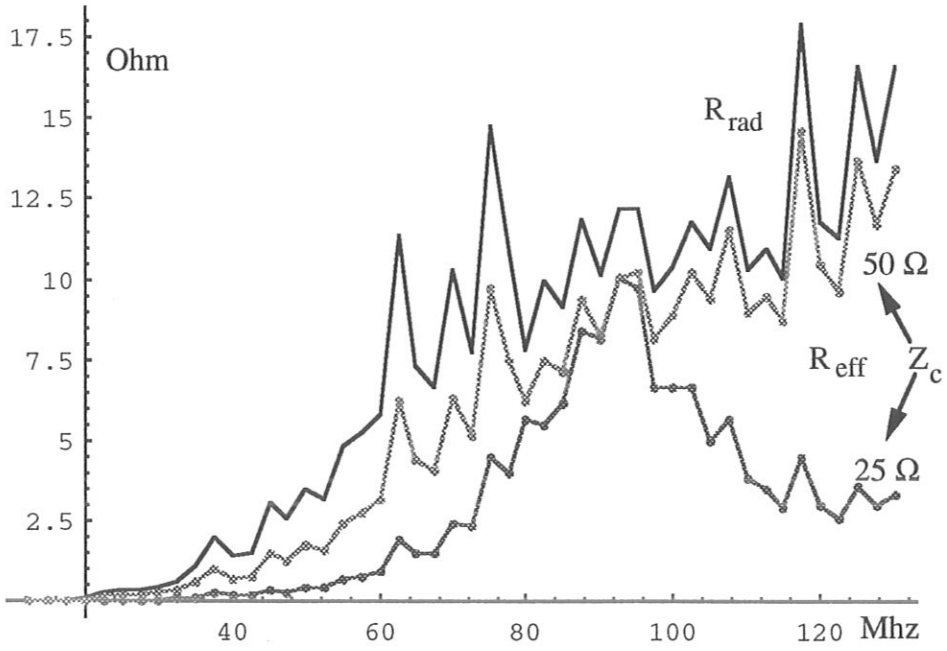

(Fig. 3c)

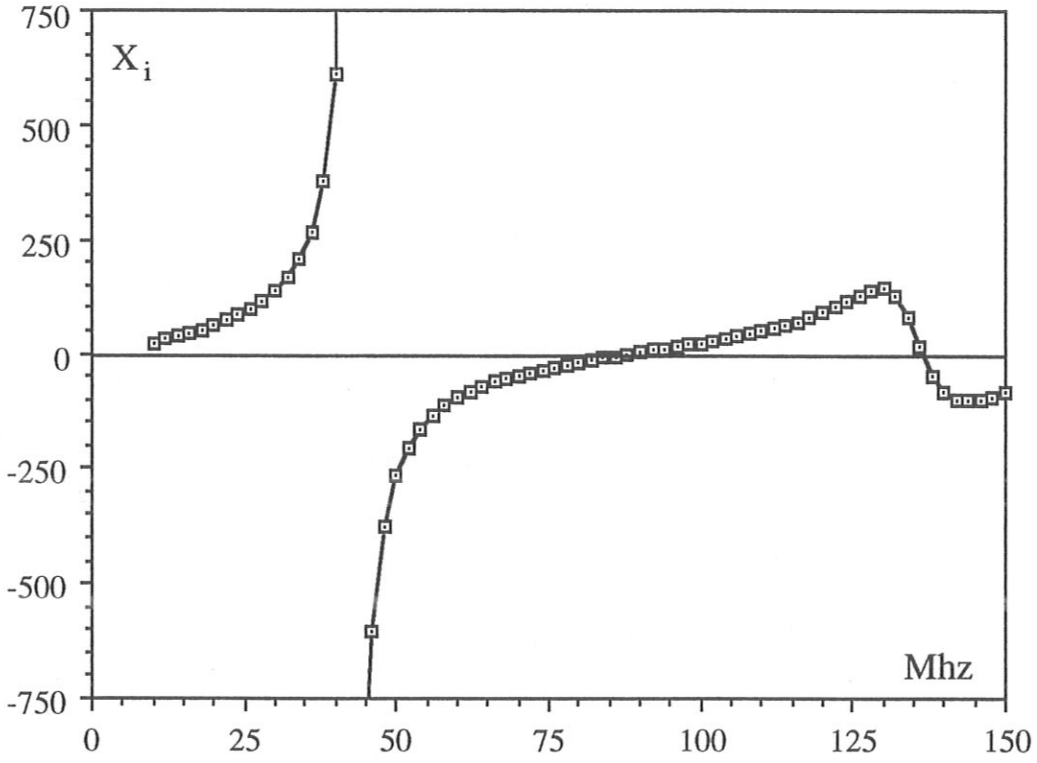
750
500
250
0
-250
-500
-750
X_i
Mhz
0
25
50
75
100
125
150

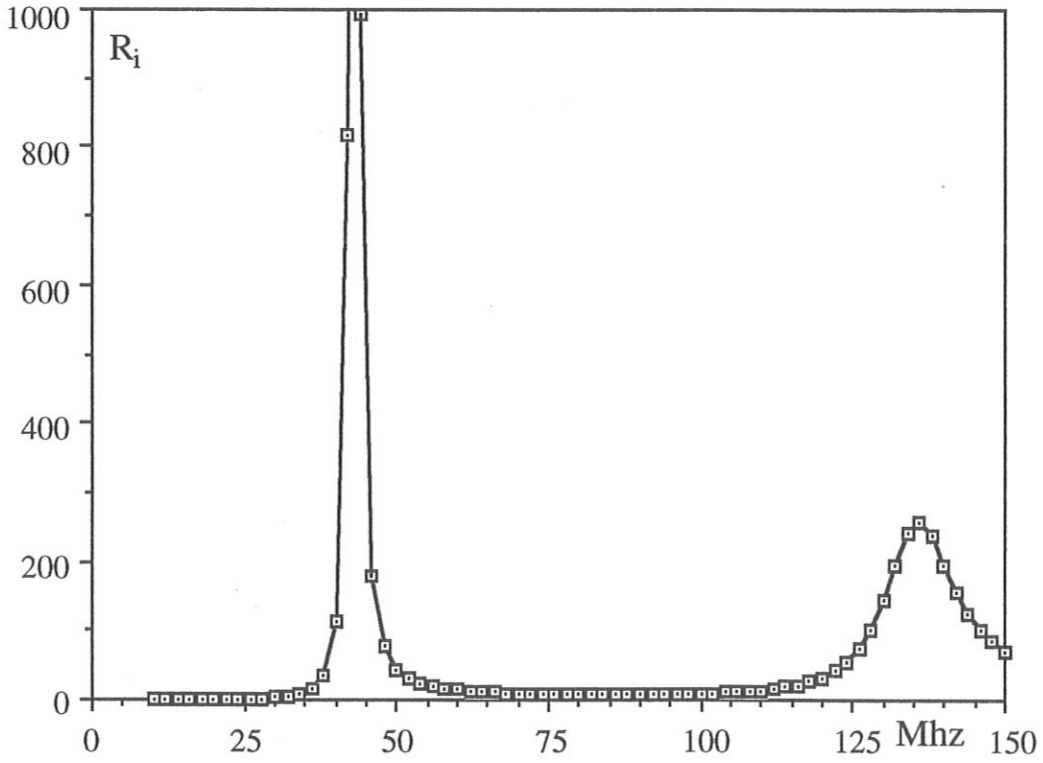
1000
800
600
400
200
0
R_i
0
25
50
75
100
125
Mhz
150

(Fig. 4 a,b)

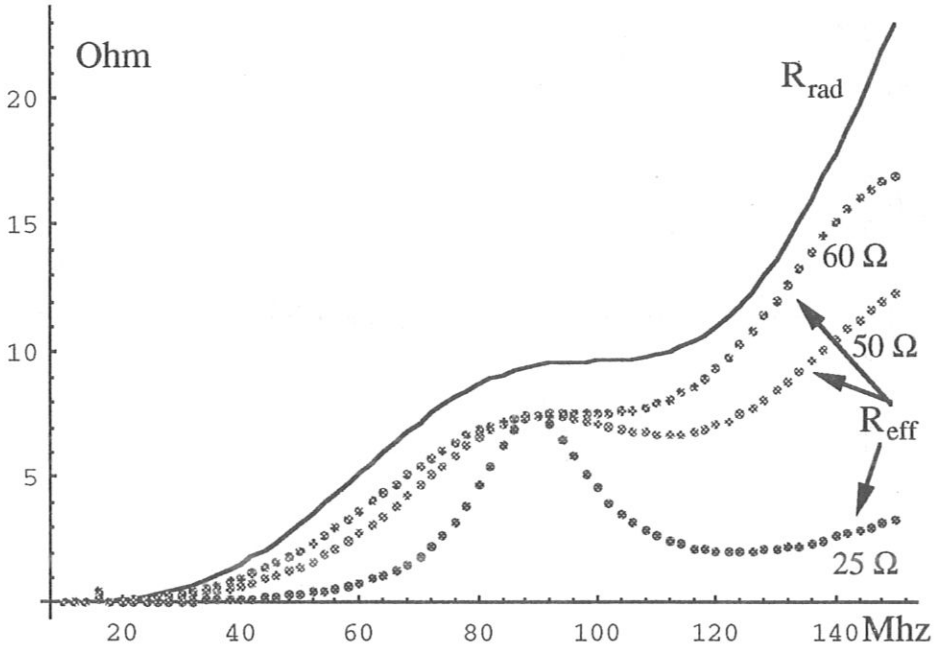

(Fig. 4c)

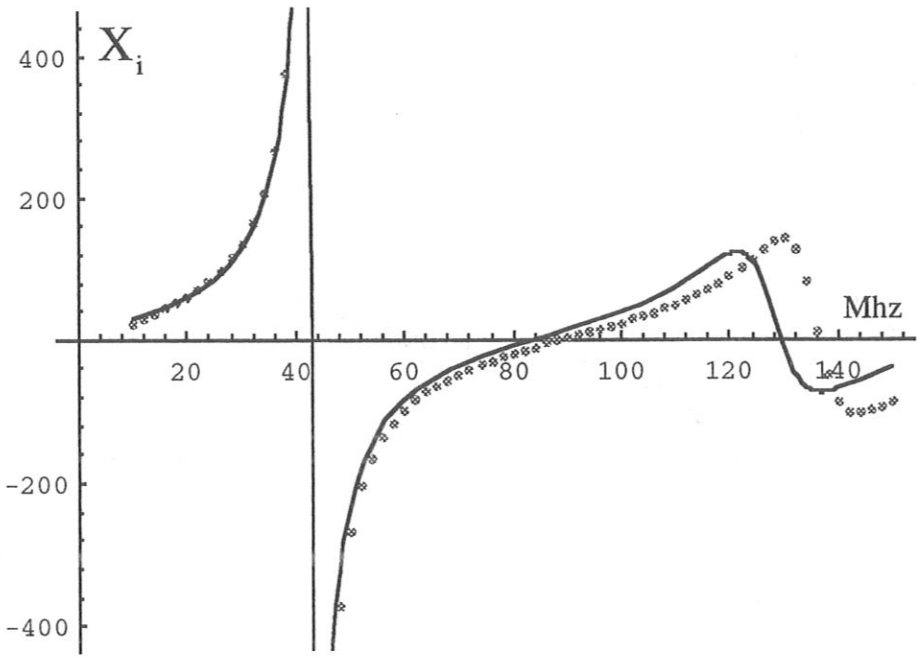
X_i
400
200
-200
-400
Mhz
20
40
60
80
100
120
140

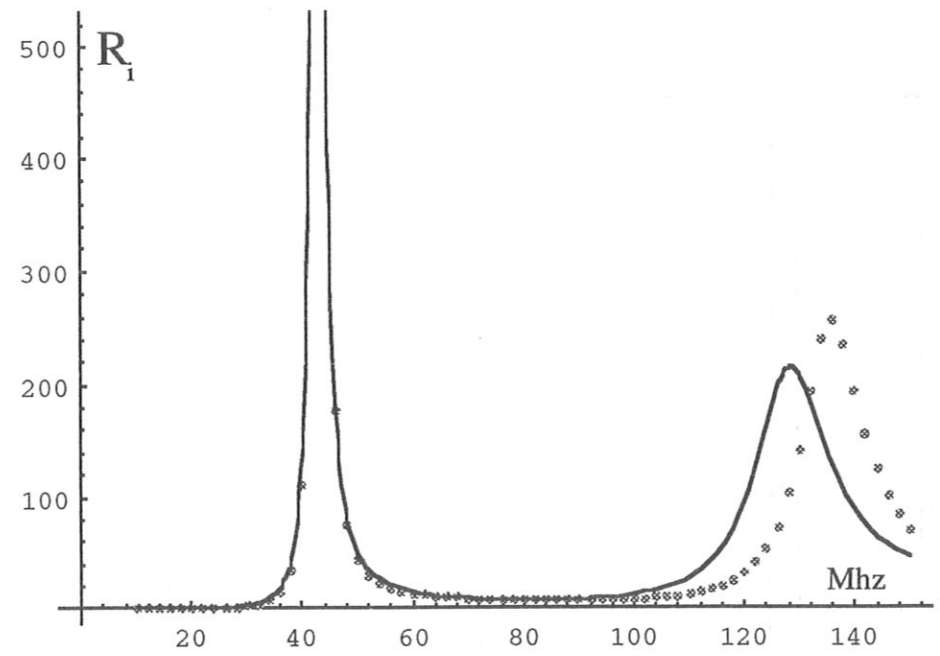
R_i
500
400
300
200
100
Mhz
20
40
60
80
100
120
140

(Fig. 5)

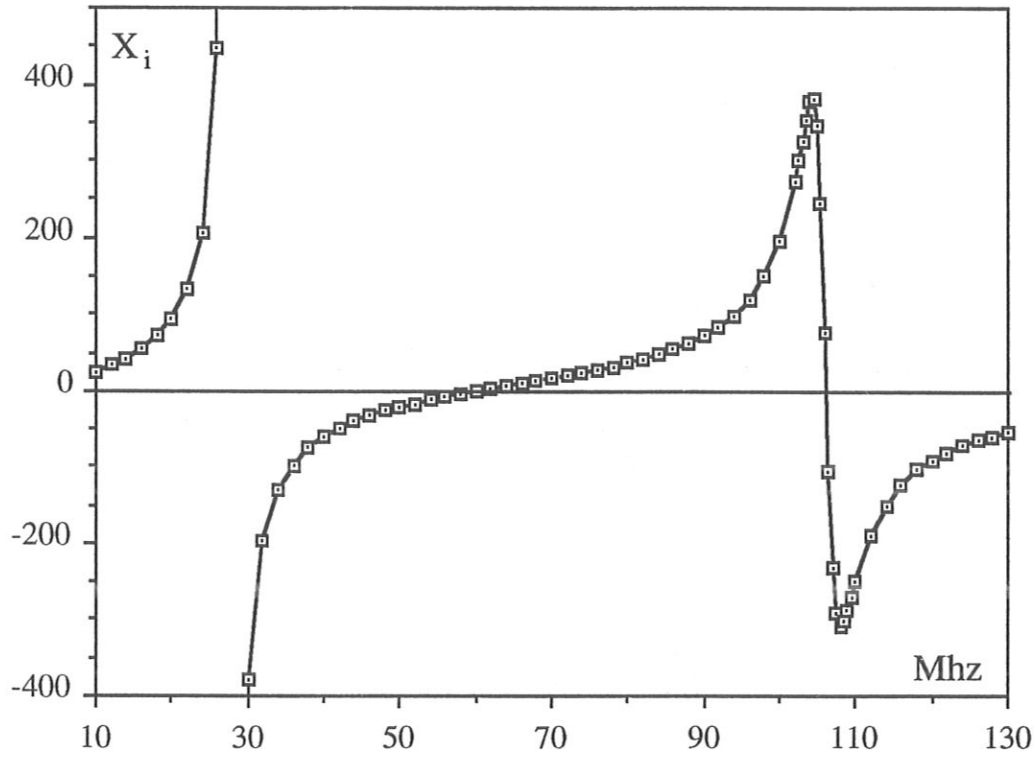
X_i
400
200
0
-200
-400
Mhz
10
30
50
70
90
110
130

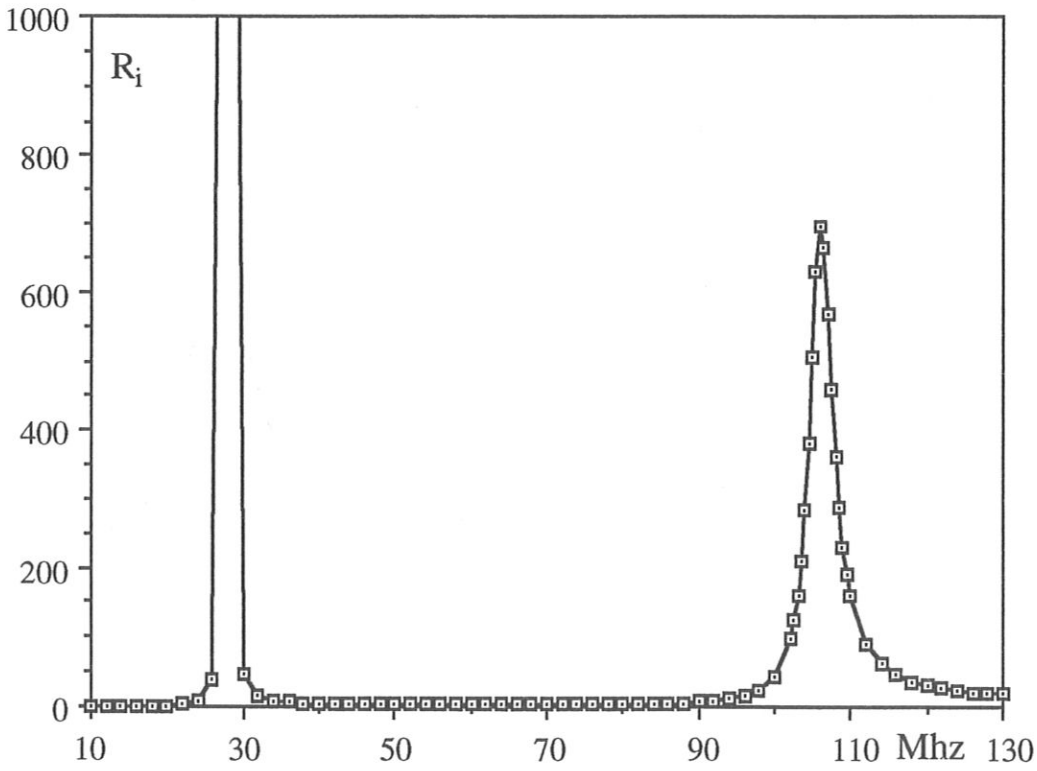
R_i
1000
800
600
400
200
0
10
30
50
70
90
110
Mhz
130

(Fig. 6 a,b)

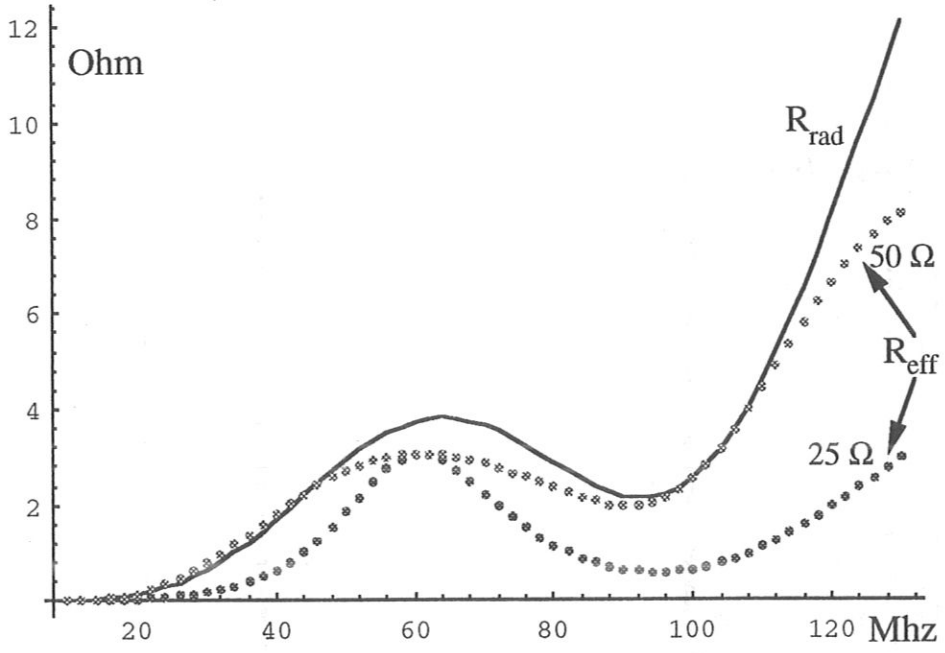

Fig. 6 (c)

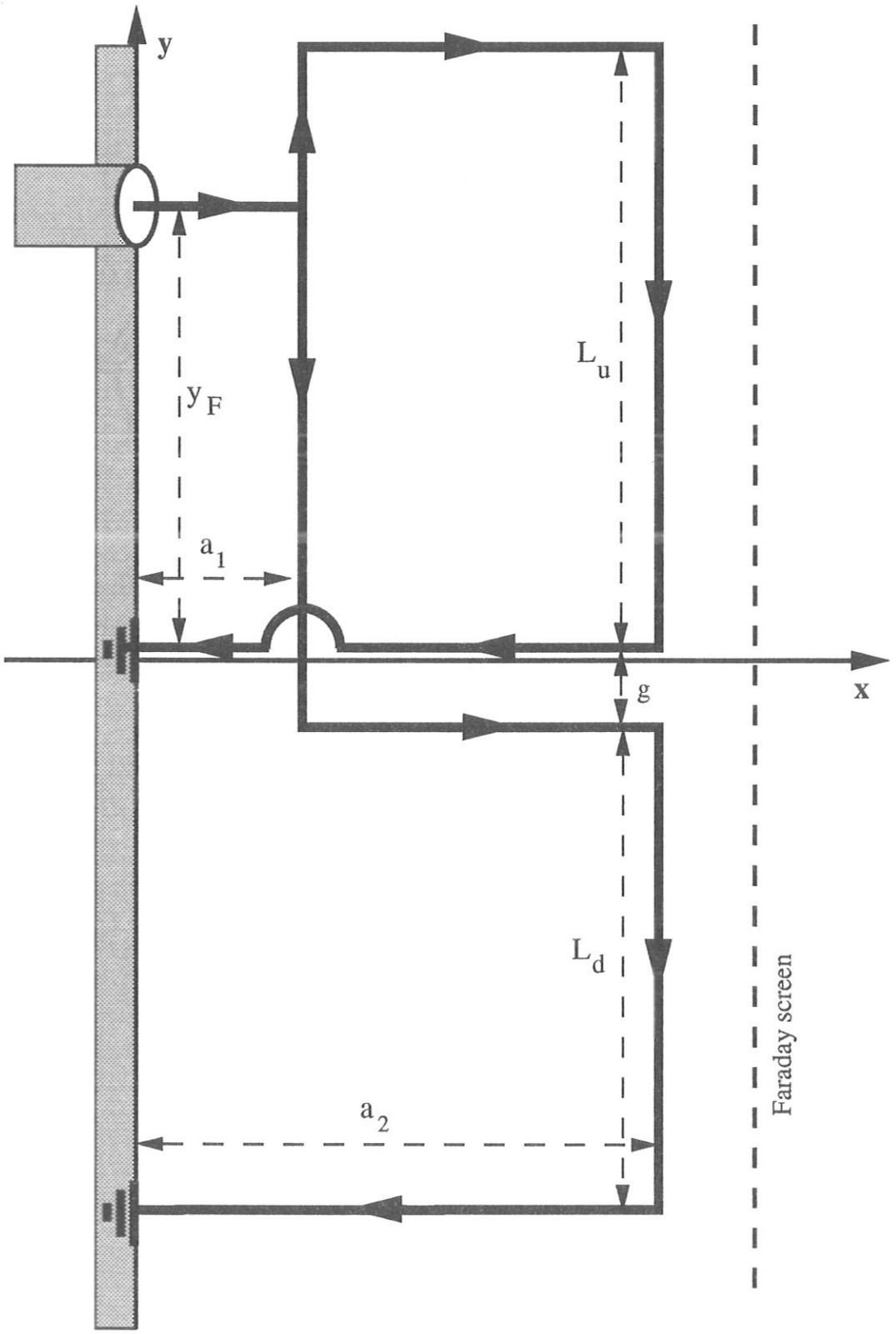

(Fig. 7)

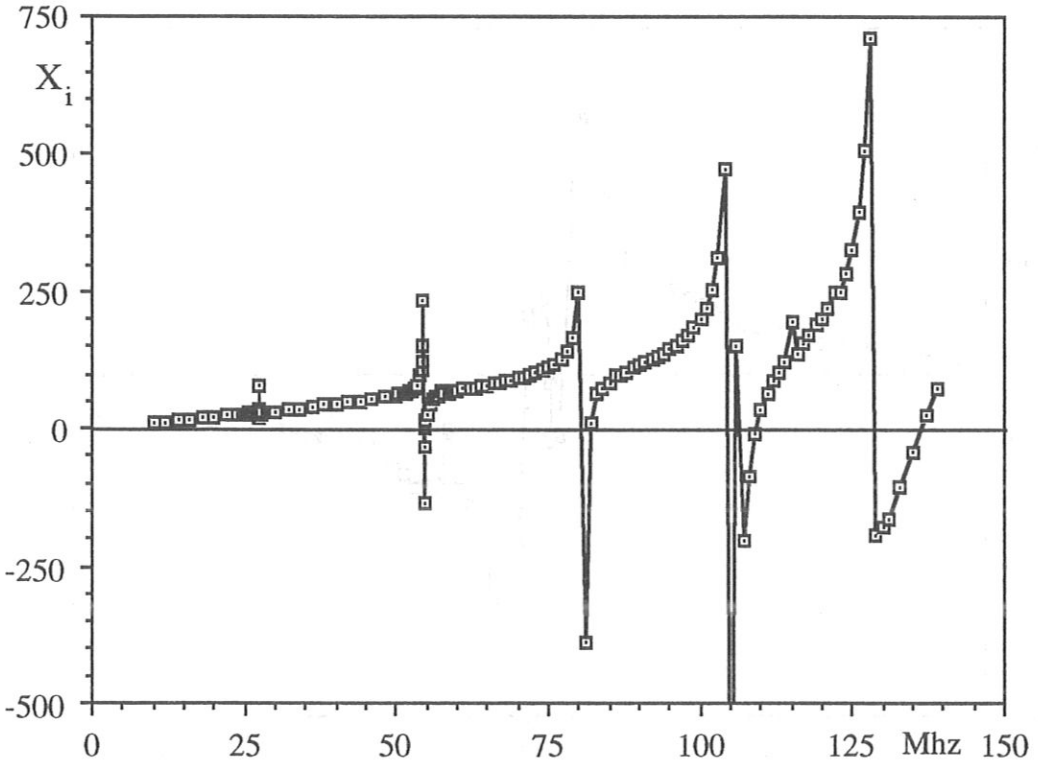
750
X_i
500
250
0
-250
-500
0
25
50
75
100
125
Mhz
150

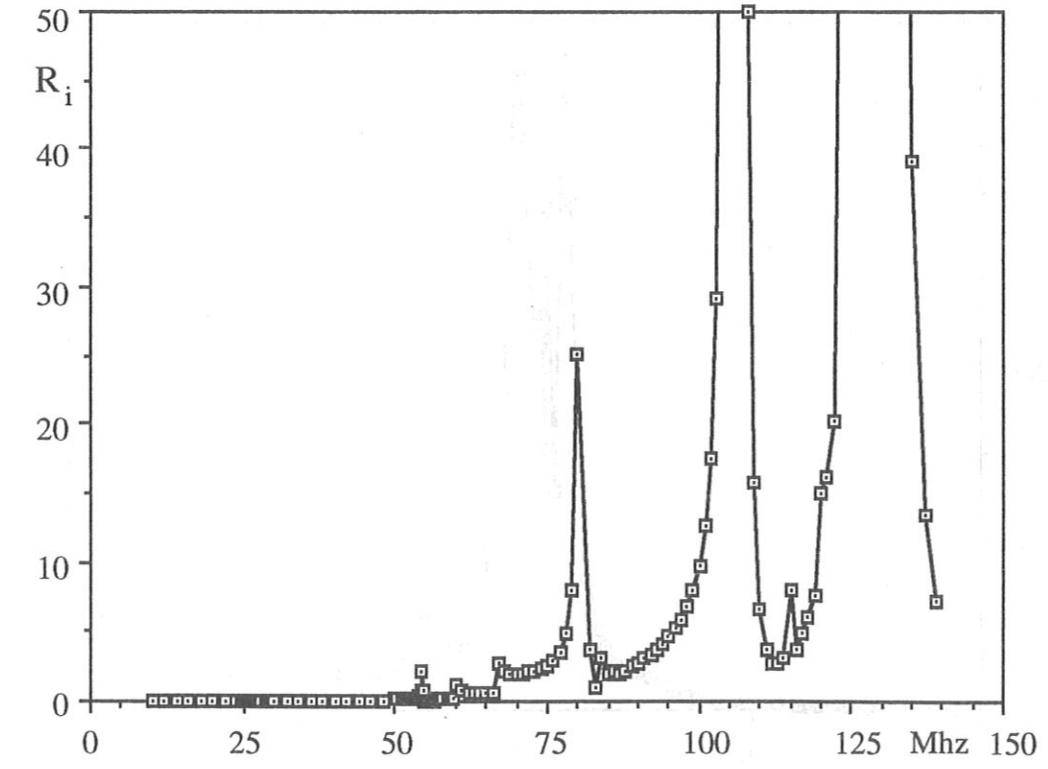
50
R_i
40
30
20
10
0
0
25
50
75
100
125
Mhz
150

(Fig. 8)

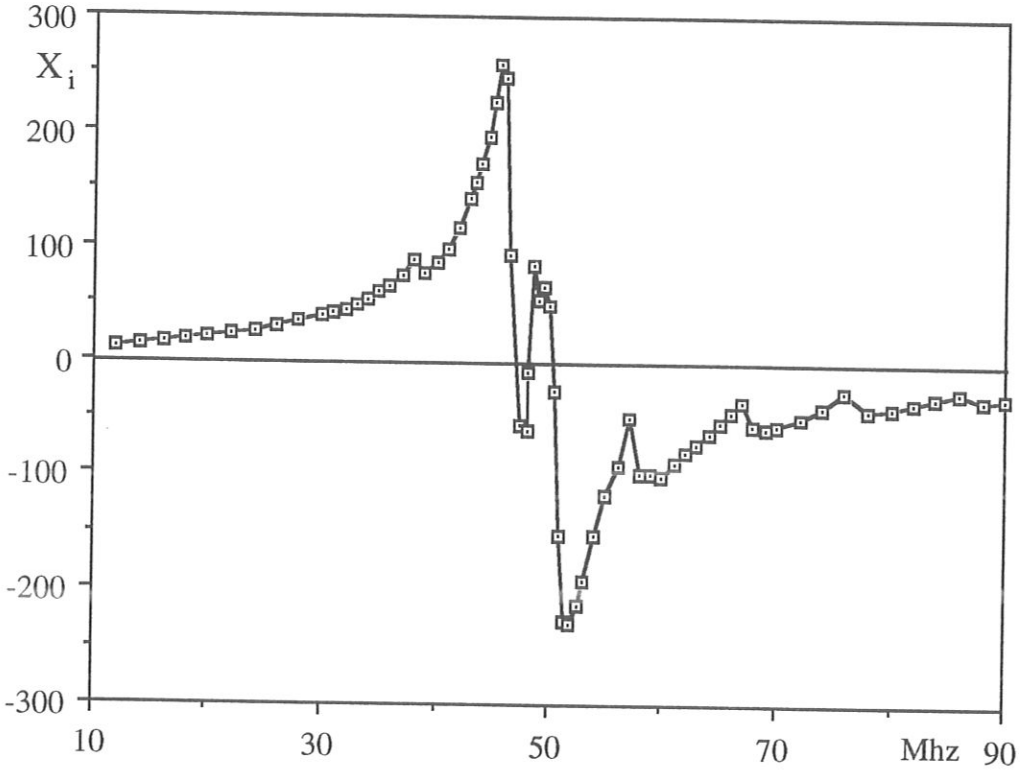
300
X_i
200
100
0
-100
-200
-300
10
30
50
70
Mhz
90

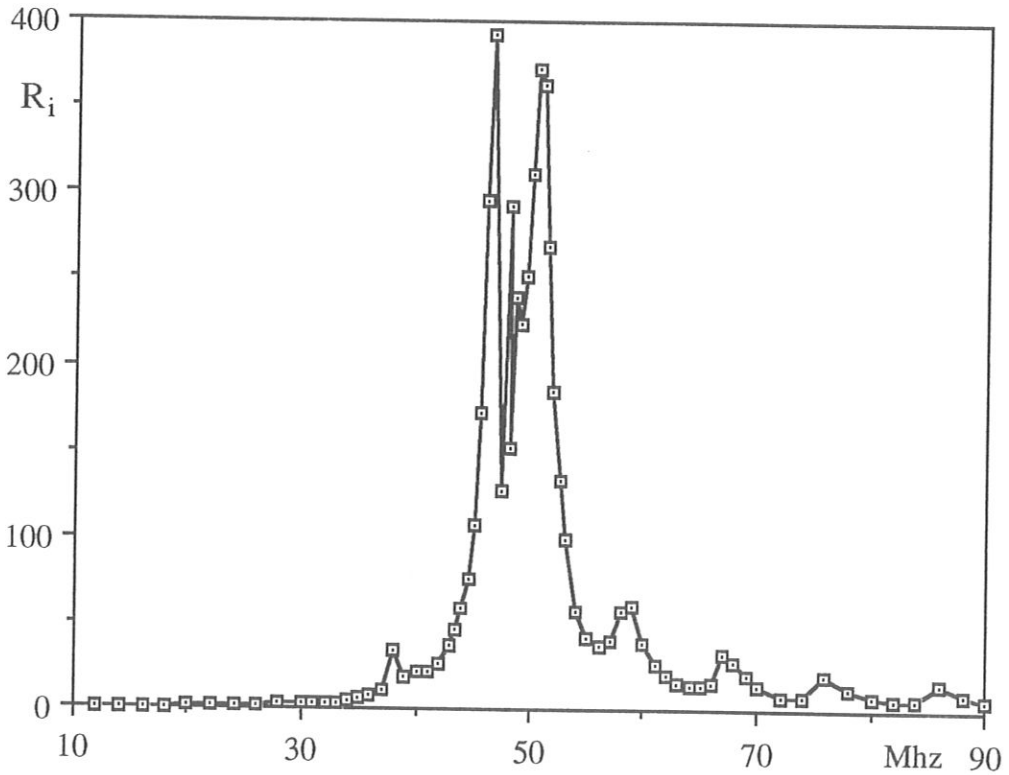
400
R_i
300
200
100
0
10
30
50
70
Mhz
90

(Fig. 9)

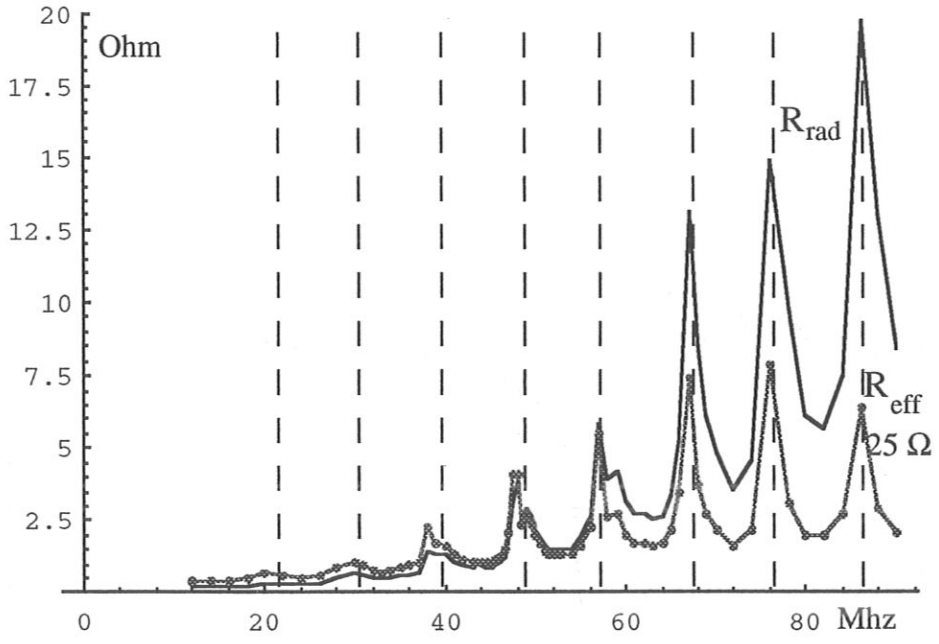

(Fig. 9c)

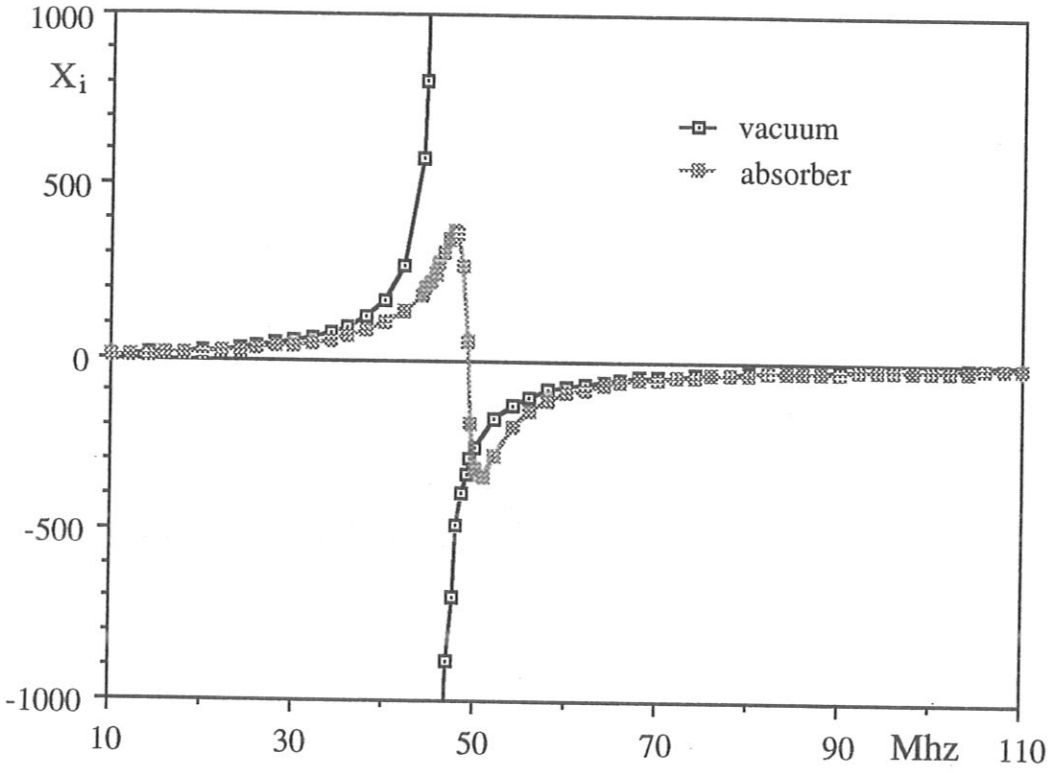
1000
X_i
500
0
-500
-1000
10
30
50
70
90
Mhz
110
vacuum
absorber

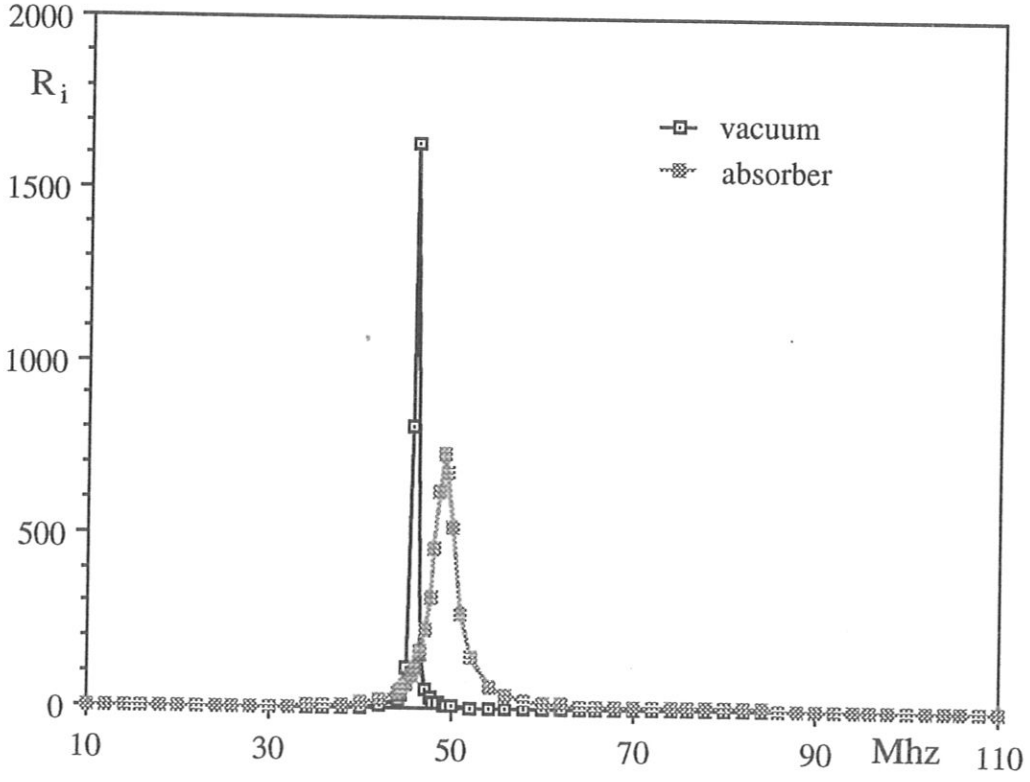
2000
R_i
1500
1000
500
0
10
30
50
70
90
Mhz
110
vacuum
absorber

(Fig. 10)

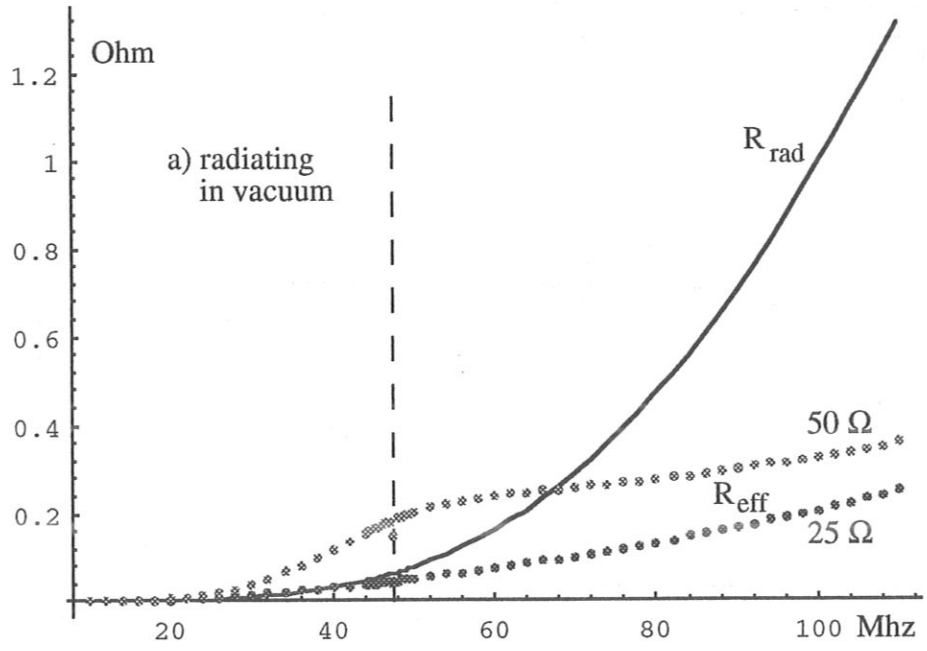
Ohm
1.2
1
0.8
0.6
0.4
0.2
a) radiating
in vacuum
R rad
50 Ω
R eff
25 Ω
20
40
60
80
100 Mhz

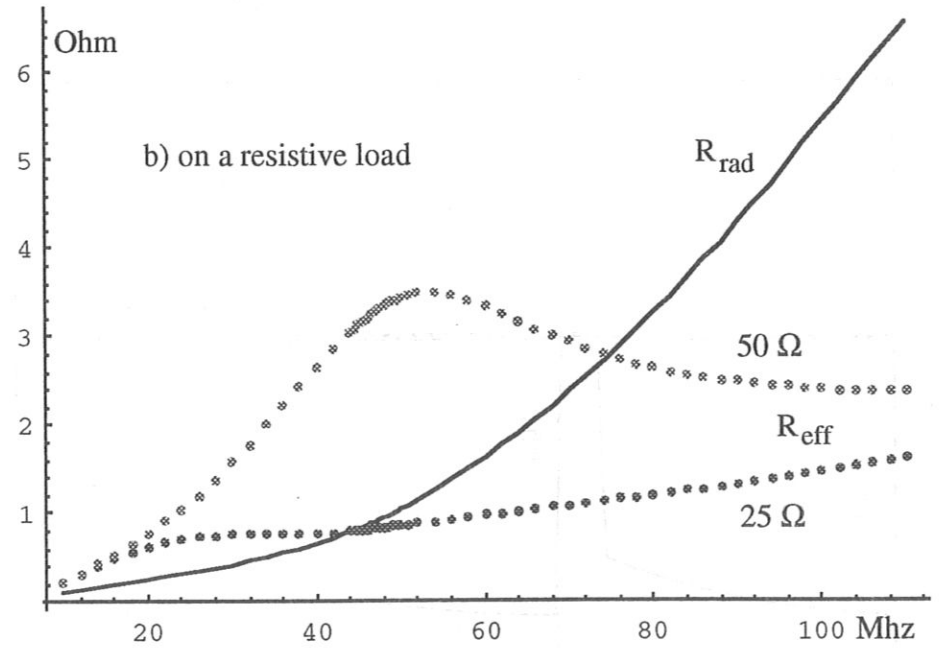
Ohm
6
5
4
3
2
1
b) on a resistive load
R rad
50 Ω
R eff
25 Ω
20
40
60
80
100 Mhz

(Fig. 11)

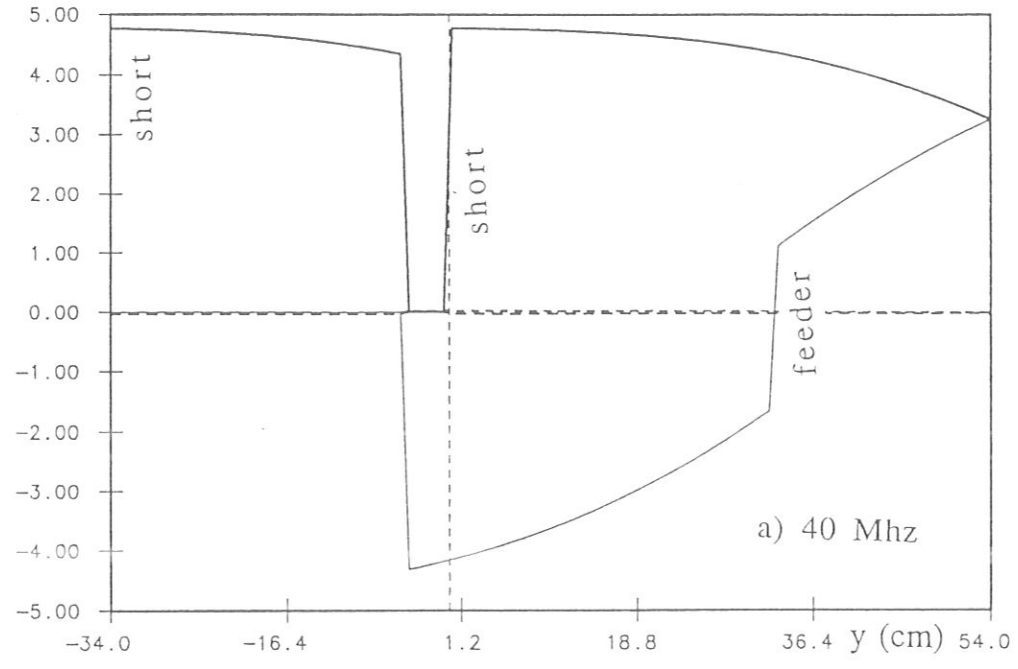
5.00
4.00
3.00
2.00
1.00
0.00
-1.00
-2.00
-3.00
-4.00
-5.00
short
short
feeder
a) 40 Mhz
-34.0
-16.4
1.2
18.8
36.4
y (cm)
54.0

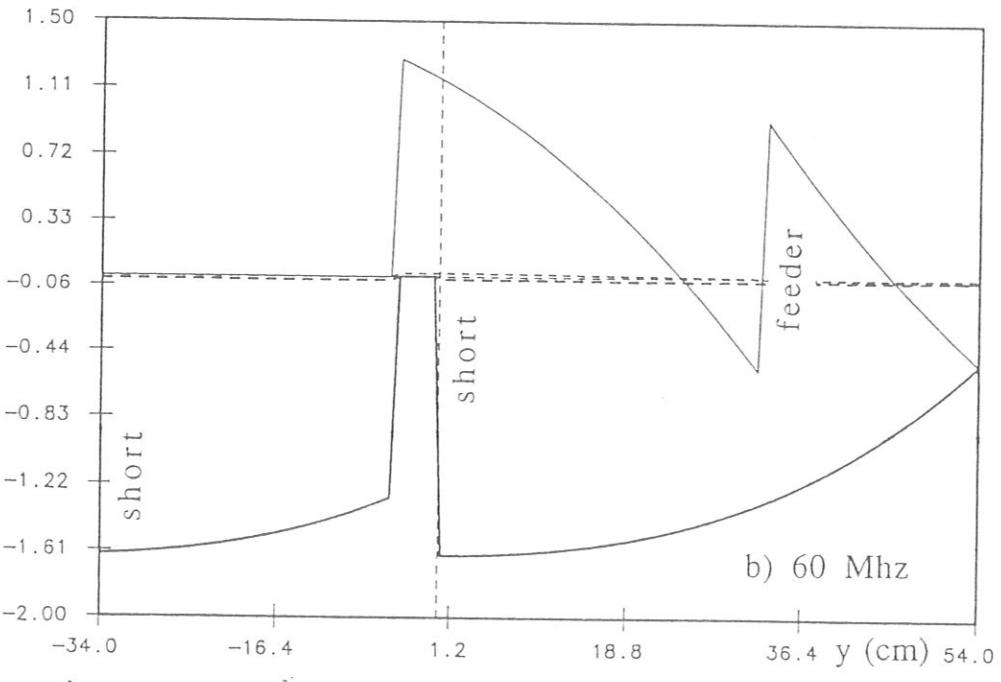
1.50
1.11
0.72
0.33
-0.06
-0.44
-0.83
-1.22
-1.61
-2.00
short
short
feeder
b) 60 Mhz
-34.0
-16.4
1.2
18.8
36.4
y (cm)
54.0

(fig. 12)

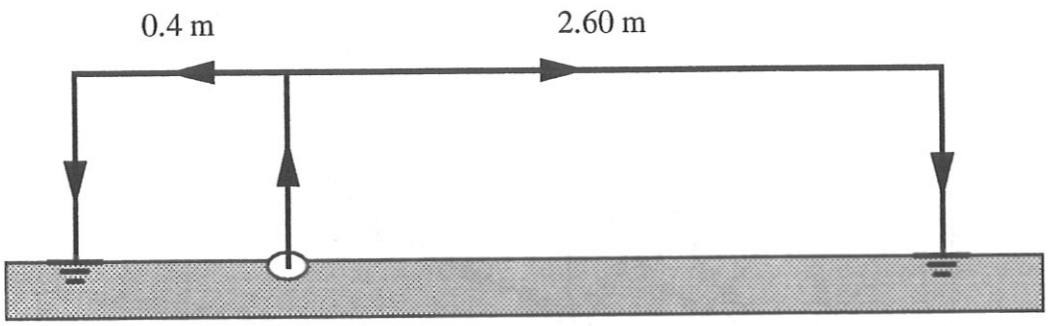

(Fig. 13)

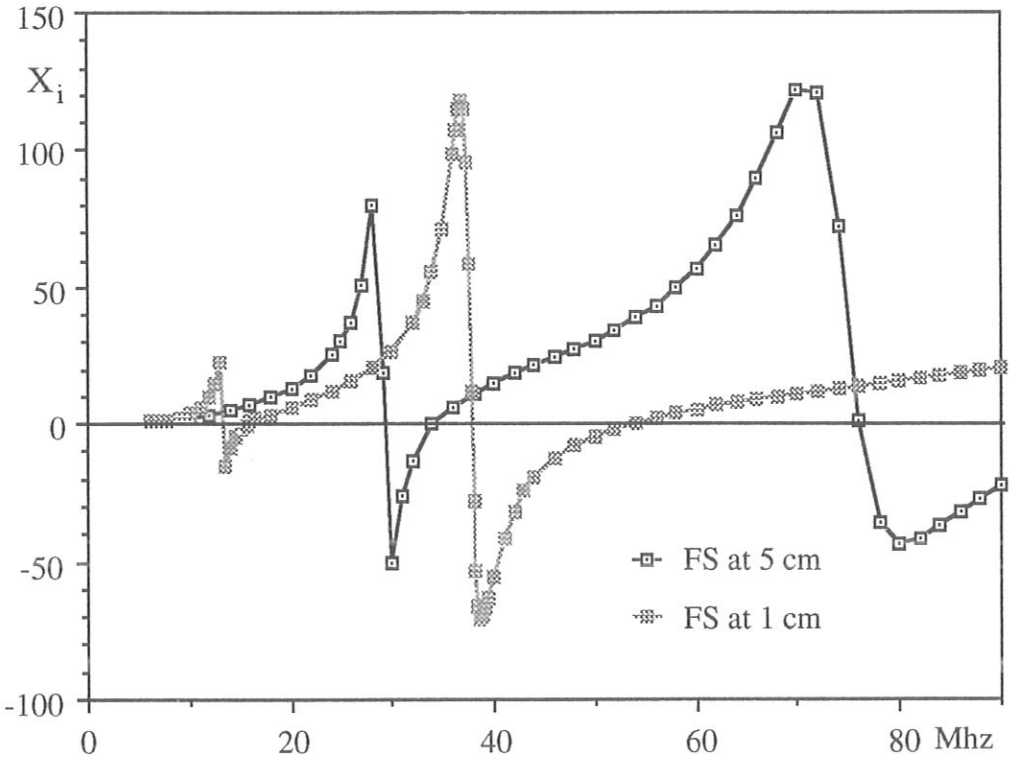
150
X_i
100
50
0
-50
-100
0
20
40
60
80 Mhz
FS at 5 cm
FS at 1 cm

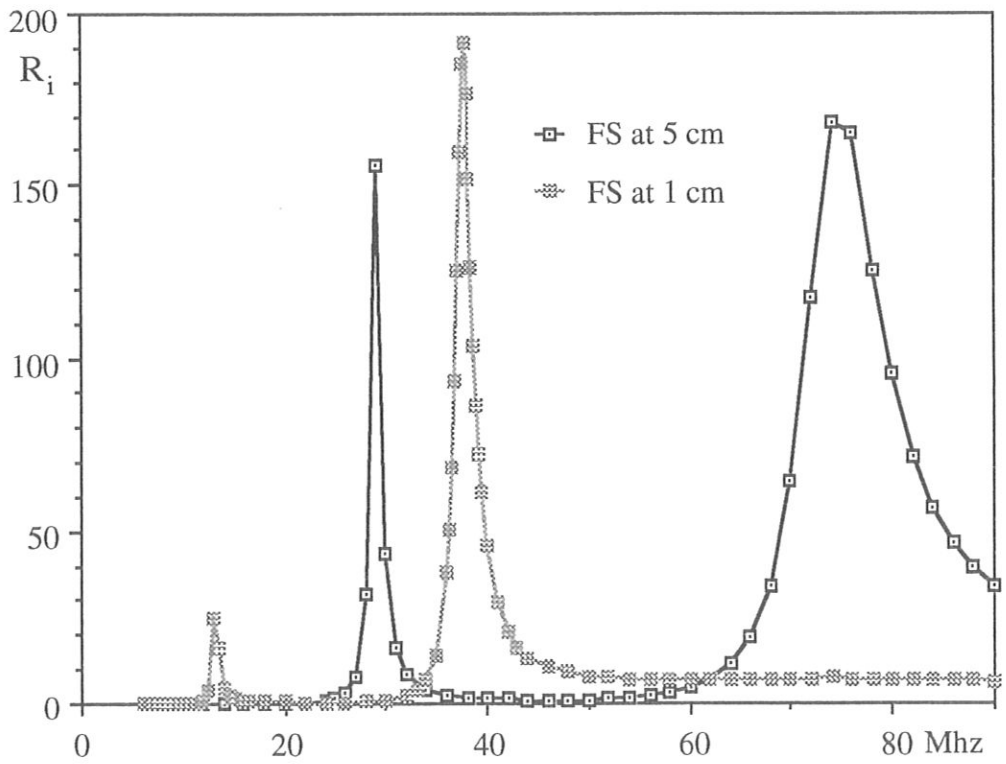
200
R_i
150
100
50
0
0
20
40
60
80 Mhz
FS at 5 cm
FS at 1 cm

(Fig. 14)

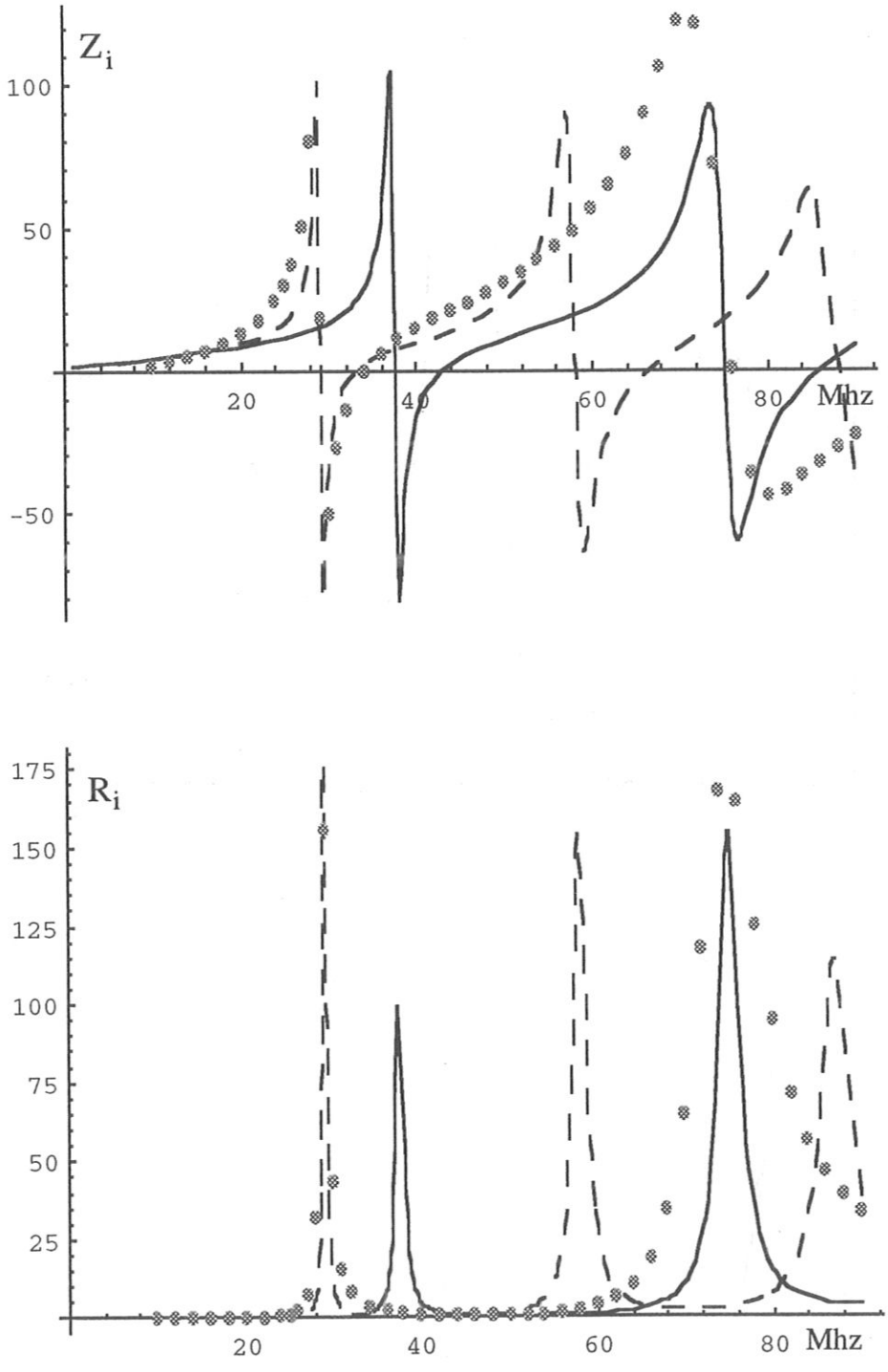
Z_i
100
50
-50
20
40
60
80
Mhz
R_i
175
150
125
100
75
50
25
20
40
60
80
Mhz

(fig. 15)

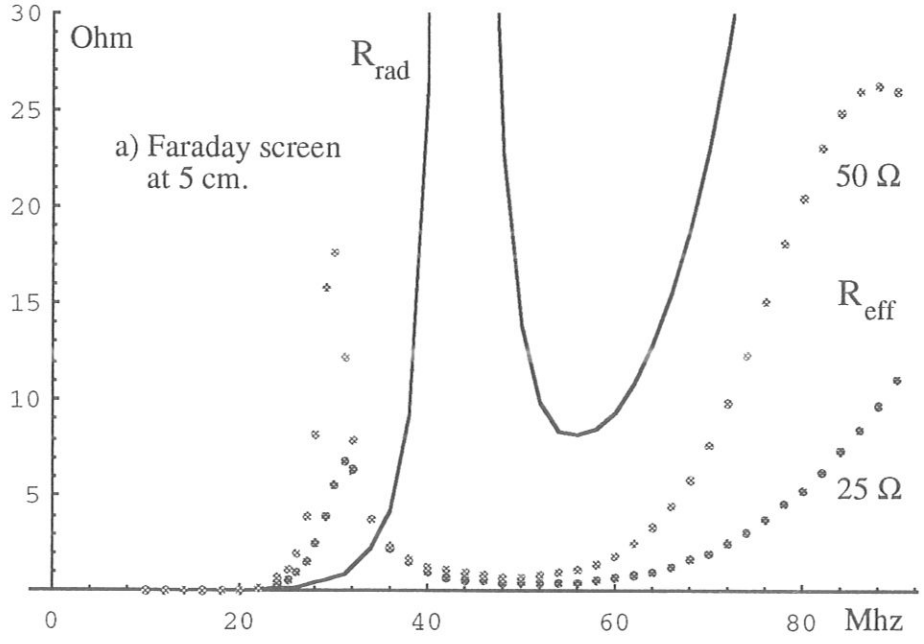
30
Ohm
25
20
15
10
5
0
20
40
60
80
Mhz
R_{rad}
a) Faraday screen
at 5 cm.
50 Ω
R_{eff}
25 Ω

(Fig. 16)

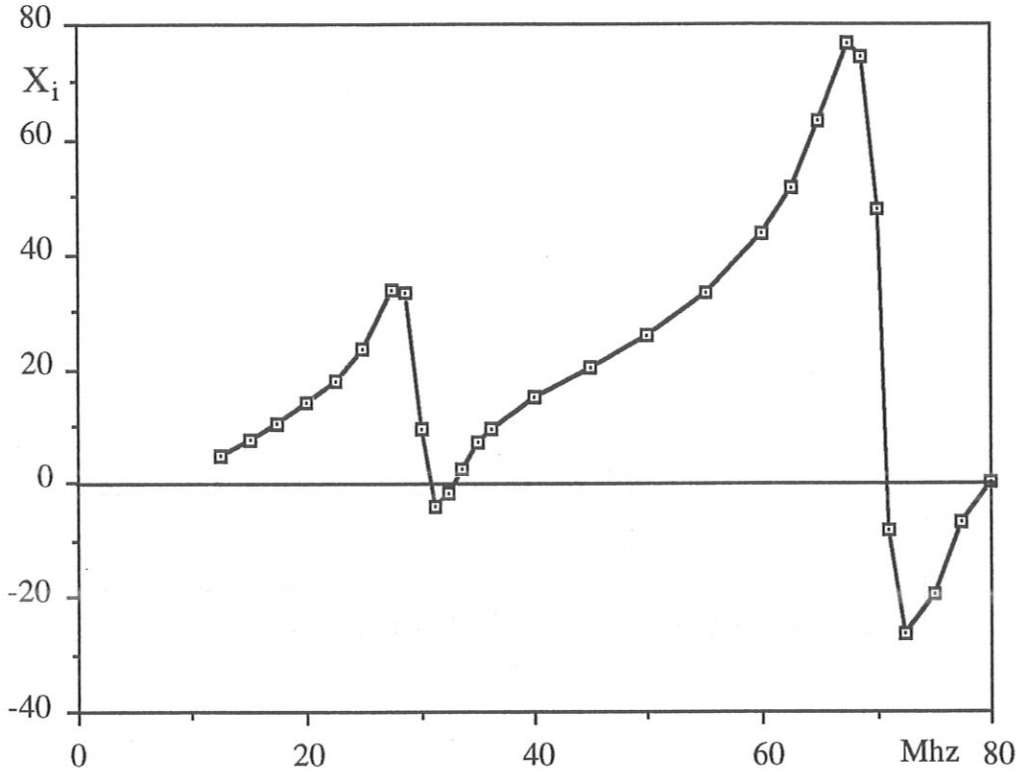
80
X_i
60
40
20
0
-20
-40
0
20
40
60
Mhz
80

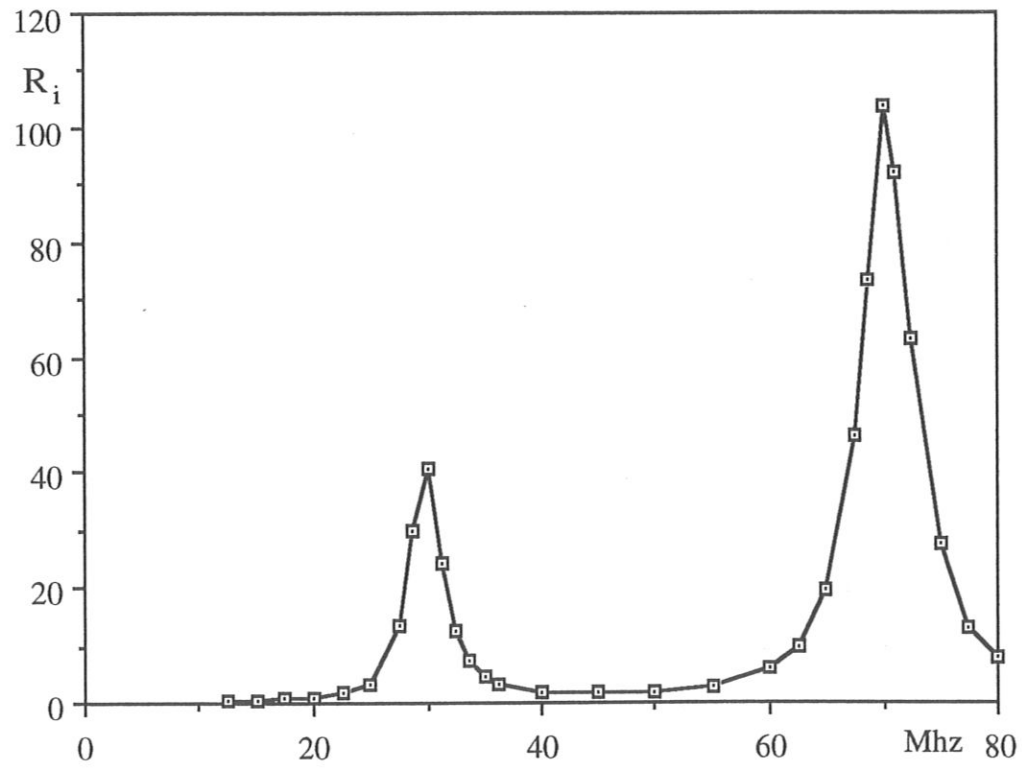
120
R_i
100
80
60
40
20
0
0
20
40
60
Mhz
80

(fig. 17 a,b)

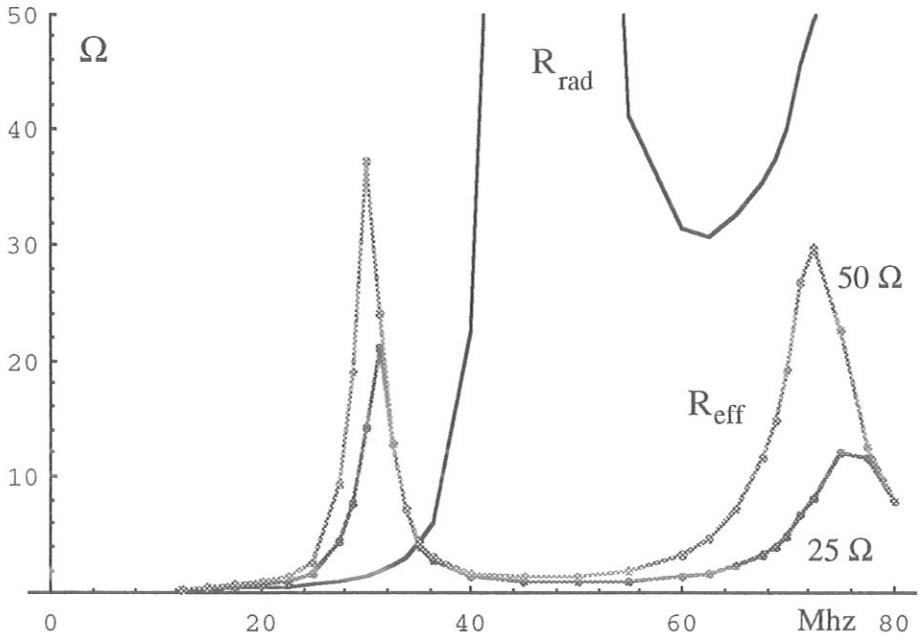

(fig. 17 c)

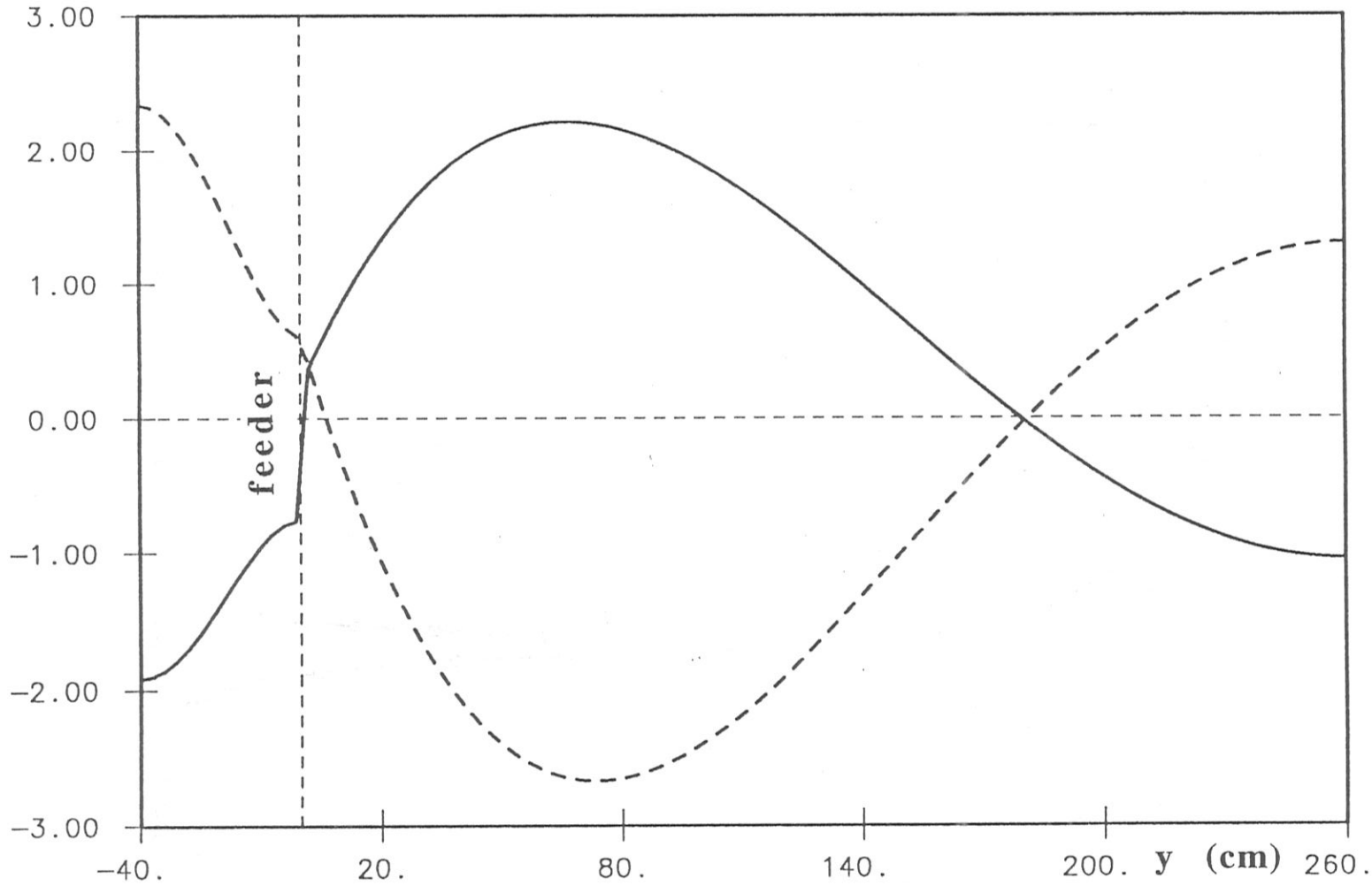

(fig. 18)

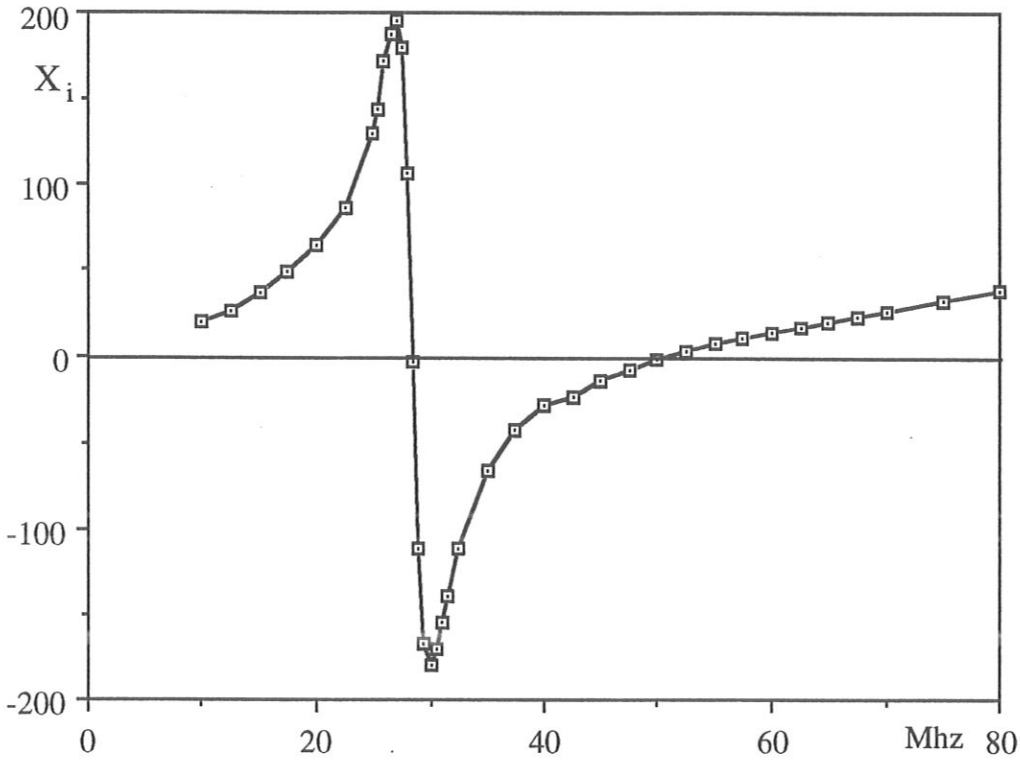
200
X_i
100
0
-100
-200
0
20
40
60
Mhz
80

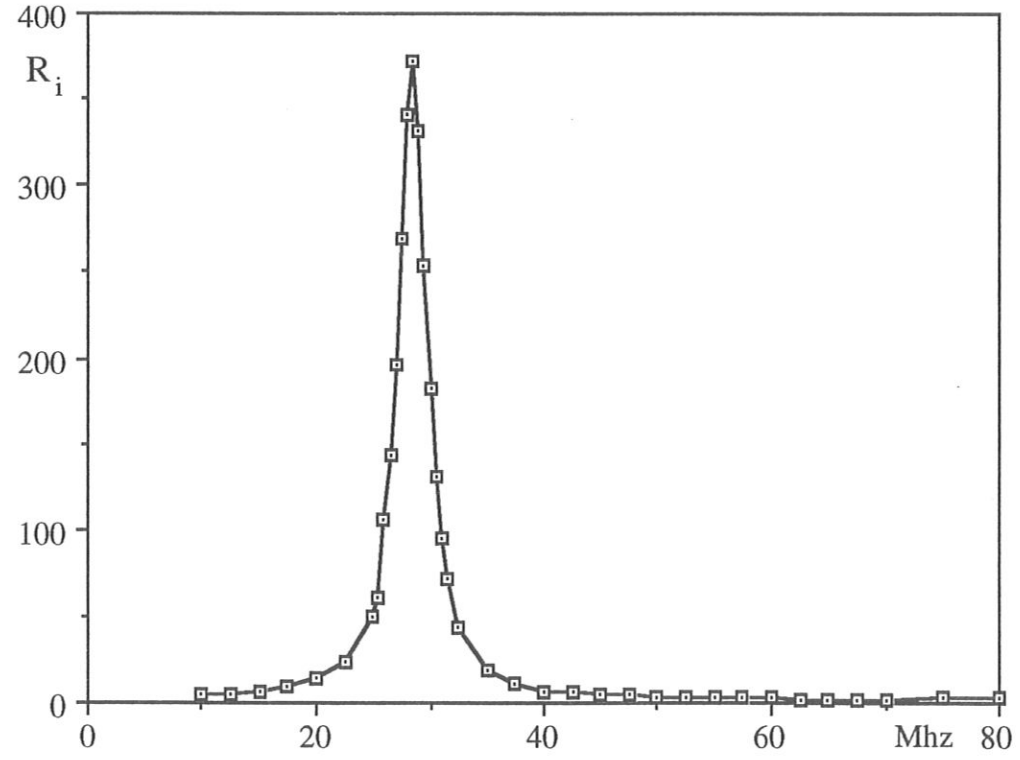
400
R_i
300
200
100
0
0
20
40
60
Mhz
80

(Fig. 19 a,b)

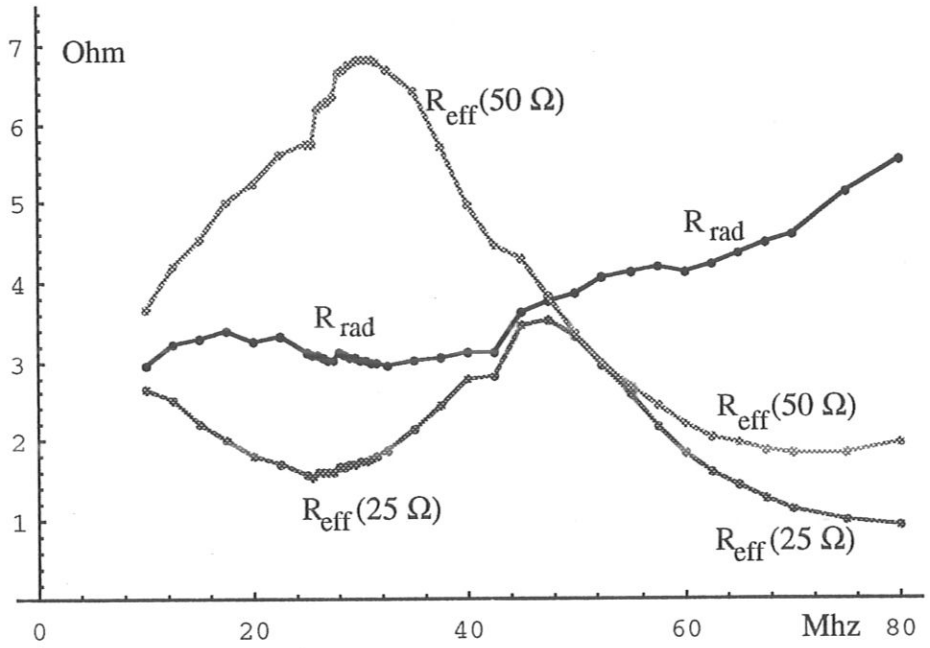
Ohm
7
6
5
4
3
2
1
R_{eff}(50 Ω)
R_{rad}
R_{rad}
R_{eff}(50 Ω)
R_{eff}(25 Ω)
R_{eff}(25 Ω)
0
20
40
60
Mhz
80

(Fig. 19 c)

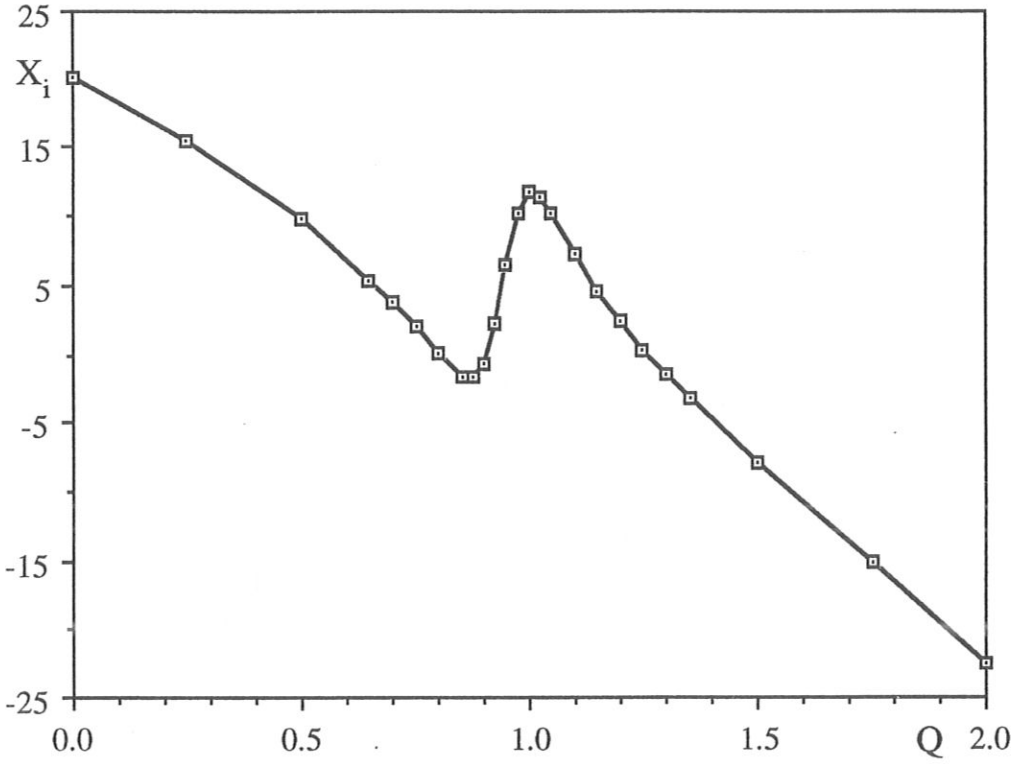

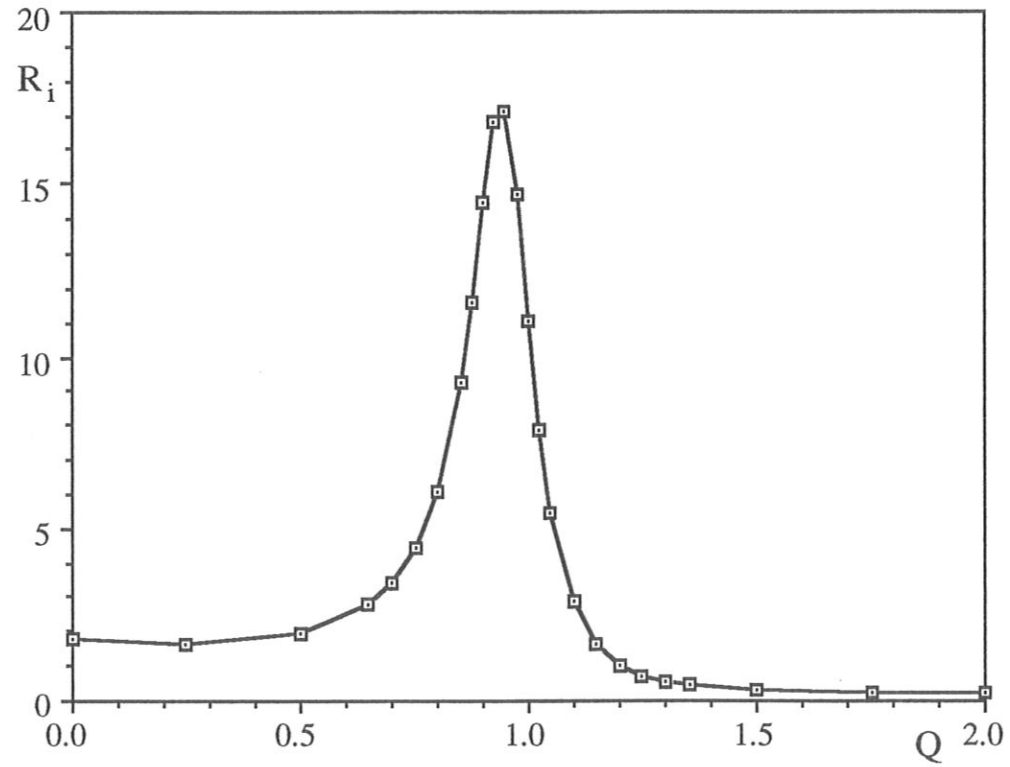

(Fig. 20 a,b)

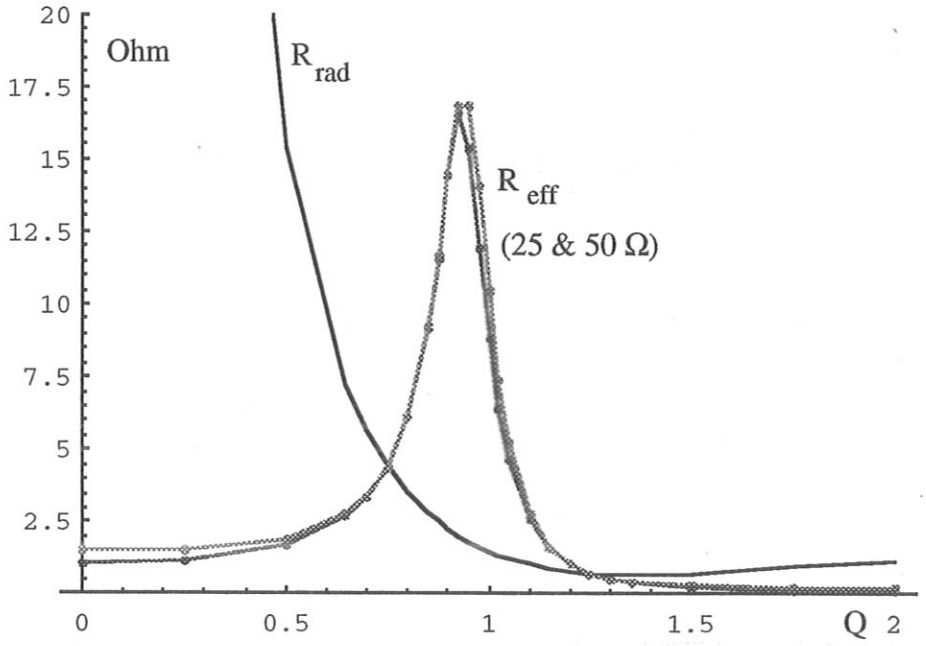

(Fig. 20 c)

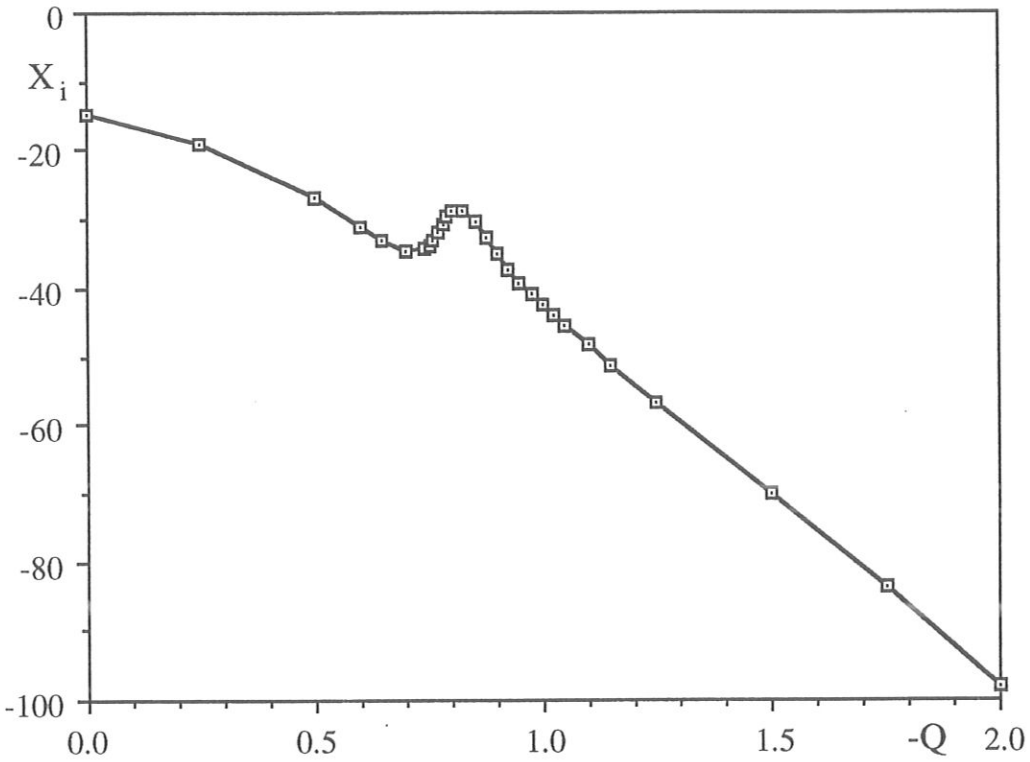

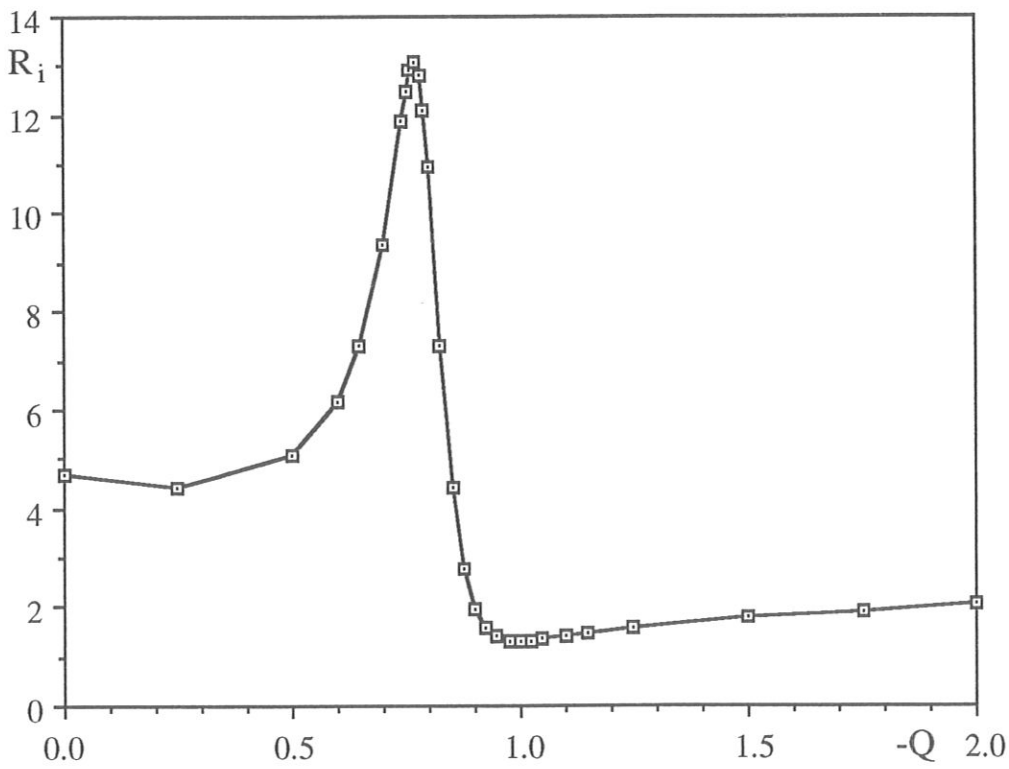

(Fig. 21 a,b)

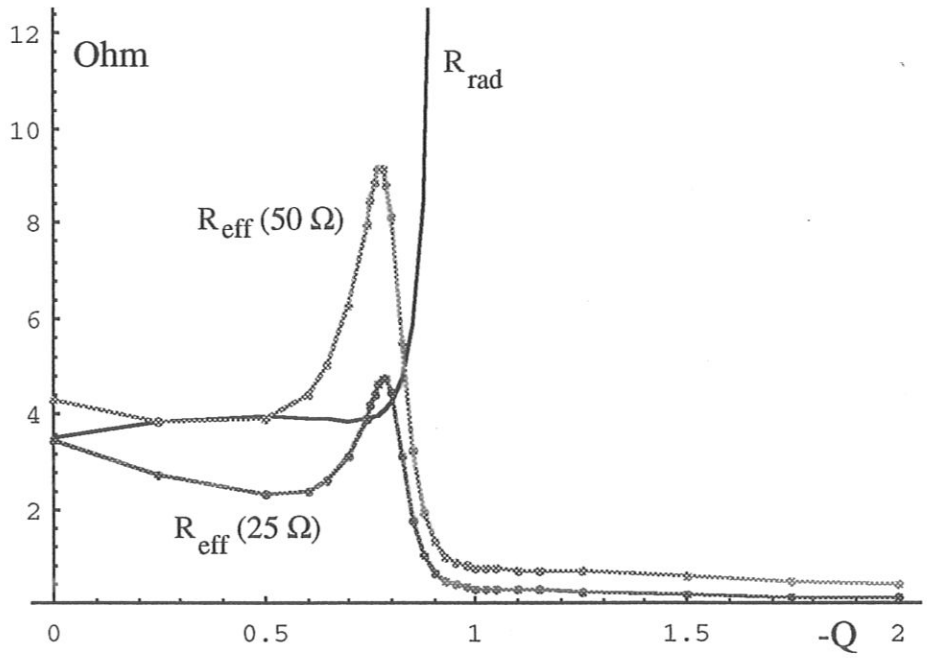

(Fig. 21 c)